Chapter 6
Laboratory Experiments

Philippe Gouze, Katriona Edlmann, Christopher Ian McDermott and Linda Luquot

Abstract The hydro-thermo-mechanical and chemical properties of reservoir rocks and the surrounding sealing units are important data for assessing the performance of a CO_2 storage. Laboratory measurements on rock samples are the first method to assess these properties and evaluate the reservoir injectivity and storage potential. Beyond standard techniques, this chapter also presents state of the art laboratory experiments capable of reproducing the in situ conditions during CO_2 injection. In addition, these methods are also used to investigate the coupling between the hydro-thermo-mechanical and chemical properties.

6.1 Introduction

The hydro-thermo-mechanical and chemical properties of reservoir rocks and the surrounding sealing units are crucial data for assessing the performance of a CO_2 storage. Laboratory measurements on rock samples are the first method to assess these properties and evaluate the reservoir injectivity and storage potential. Then laboratory experiments reproducing the conditions of CO_2 injection can be performed for characterizing the mechanisms of alteration of these properties and for

P. Gouze (✉)
Géosciences, Université de Montpellier, CNRS, 34095 Montpellier Cedex 5, France
e-mail: philippe.gouze@univ-montp2.fr

K. Edlmann
School of Geosciences, University of Edinburgh, Edinburgh, UK
e-mail: katriona.edlmann@ed.ac.uk

C.I. McDermott
School of Geoscience, Edinburgh Collaborative of Subsurface Science and Engineering (ECOSSE), University of Edinburgh, Edinburgh, UK
e-mail: cmcdermo@staffmail.ed.ac.uk

L. Luquot
Spanish National Research Council (IDAEA-CSIC), 08034 Barcelona, Spain
e-mail: linda.luquot@iqac.csic.es

A. Niemi et al. (eds.), *Geological Storage of CO_2 in Deep Saline Formations*,
Theory and Applications of Transport in Porous Media 29,
DOI 10.1007/978-94-024-0996-3_6

determining the input parameters for predictive modeling. This chapter presents a panel of methods and procedures of laboratory testing of rock and fluid samples that can be applied during the exploration phase when boreholes are drilled and core samples retrieved.

The properties of the geomaterials forming the storage system—the reservoir and the caprock—prior to the CO_2 injection are usually determined in the laboratory using samples cored while drilling the wells or samples taken from quarries or other cored sites considered to be similar. Also, the changes of these properties, triggered by the injection of CO_2, can be assessed by laboratory experiments reproducing the dynamic processes taking place during the different stages of the storage and by studying geological systems that have been exposed to natural CO_2 flooding. The well cement annulus that plays a key role in the storage confinement is also an important component of the storage system.

The methods applied for measuring the properties of the storage system within the framework of CO_2 sequestration projects are to a large extent similar to those routinely performed in oil and gas industry during the exploration of hydrocarbon reservoirs. For instance, the characterization of the reservoir rock involves standard investigations including petrographic characterization as well as the measurement of hydrodynamic and mechanical properties. Basic properties such as porosity, thermal conductivity, permeability and most of the mechanical properties require a set of specific measurement tools that are relatively simple and similarly implemented in many academic and industrial research institutes. Standard laboratory measurements are also employed to determine fluid properties such as viscosity and solubility for mixtures involving several components and phases. Conversely, the evaluation of properties such as relative permeability (for parameterizing the flow of two or several fluid phases) and mineral reactivity requires more complex experimental protocols. They involve several steps and often rely on empirical model and on the knowledge of some other properties related to the pore structure, rock composition and fluid composition. Nevertheless these measurements follow procedures that are quite well established and widely used, albeit each team may operate alternative protocols.

Beside these basic measurements, CO_2 underground storage triggered additional challenges and promoted the development of new laboratory tools. Research activities related to the injection of CO_2 in reservoir, and consequently the development of specific laboratory tools and protocols, were first initiated in the frame of the development of enhanced oil and gas recovery using CO_2. The specificity of CO_2 underground storage compared to standard oil and gas industrial activities is twofold. First CO_2 storage involves filling geological reservoirs with a fluid that is potentially chemically aggressive and may cause strong and often irreversible alterations of the storage system hydrodynamic and mechanical properties. Second, the steric, thermic and dynamic effects, including buoyancy forces, caused by the massive injection of supercritical CO_2 ($scCO_2$) may alter the mechanical properties of the reservoir and cause confinement failure. Thus, the characterization of the mechanical and chemical mechanisms that can alter the properties of the confinement is a critical issue for CO_2 underground storage. Specifically, the development

of fractures in the well cement and in the caprock layers, and the potentially induced chemical alteration processes in case of leakage of CO_2-rich brine and $scCO_2$-brine mixtures, must be investigated in detail using laboratory experiments because it is impractical to be determined at field scale.

Laboratory experiments reproducing the complex dynamic of the storage system have been developed mainly during the last decade. The main objective of these experiments is to investigate the coupled thermo-hydro-mechanical and chemical (THMC) mechanisms that are involved during the injection of the CO_2 into the reservoir. New experimental rigs allowing the simulation of the temperature, pressure, fluid composition and fluid flow conditions while measuring the effects on the change in the petrophysical, hydrodynamic and mechanical properties have been designed and constructed, for instance within the frame of the MUSTANG project. These tools have been used not only to explore the behavior of the reservoir when invaded by $scCO_2$ or CO_2—enriched brine, but also (1) to simulate leakages through fractured caprocks or damaged well cement annulus, (2) to study the efficiency of the injection of remediation fluids (healing reagents) and (3) to measure the hydro-mechanical coupling parameters during caprock fracturing.

The following sections will give an overview of the different laboratory techniques and experiments that are essential not only for parameterizing the models, but also to characterize the outcomes of complex processes that could not be easily studied at depth in the course of field tests. Yet, it is important to keep in mind that property measurements and mass transfer experiments performed in the laboratory used samples of some cubic centimeters in volume and therefore the representativeness of the results relies on the quality of the sample. The representativeness of the sample hinges on two main factors: the spatial heterogeneity of the studied geological unit and the care taken during sampling in order to minimize the alteration of the properties. The pertinent choice of the samples as well as the number of samples and measurements needed to characterize a property or a process is a critical step of the experimental protocol.

6.2 Measuring Hydrodynamical Properties

CO_2 storage in geological formations involves numerous processes at a broad range of scales. For example, at large scale and far from the injection well, fluid pressure buildup will be sensitive to large scale permeability (Birkholzer et al. 2012), whereas, at local scale, the CO_2 and brine relative permeability will control the dynamic of the system (Juanes et al. 2006). With time, CO_2 will partially dissolve into the water. This dissolution will be controlled by hydrodynamic parameters; initially by molecular diffusion and then accelerated by dispersion (Hidalgo and Carrera 2009; Riaz et al. 2006). Consequently, it is essential to evaluate all the hydrodynamical properties of the reservoir to model (1) the CO_2 dissolution rate into the water; (2) the CO_2 plume localization and (3) the fraction of CO_2 in water depending on the structural characteristics of the storage system and on the dynamic conditions enforced by the CO_2 injection.

These measurements are quite similar to those routinely performed for evaluating oil and gas reservoirs and specifically to assess the performance of enhanced oil recovery using CO_2. For instance, the theoretical aspects related to measurements of porosity, absolute permeability, electrical properties (used to evaluate tortuosity and formation factor), thermal and chemical diffusion, fluid saturation, interfacial tension, wettability, capillary pressure and relative permeability have been described in detail in several books (Dandekar 2013; Sahimi 2011; Pinder and Gray 2008). In this section we will presents briefly the objectives and methods for measuring the hydrodynamic properties of the reservoir rocks, the caprocks and the cements and then focus on their use in the frame of CO_2 underground storage where these properties may evolve with time due to chemical reactions. For instance mineral dissolution and precipitation can strongly modify pore connectivity and consequently (relative) permeability, but also the diffusivity, the reactive surface area and virtually all the properties of the material (Guarracino et al. 2014; Gouze and Luquot 2011; Luquot and Gouze 2009; Navarre-Sitchler et al. 2009; Noiriel et al. 2009).

6.2.1 Porosity and Structural Parameters

6.2.1.1 Porosity and Tortuosity

Porosity denotes the volume fraction of void in a rock. Usually there are *interconnected pores* and *isolated pores*. The former designates the fraction of the porosity in which fluid(s) can flow if a pressure gradient is applied. The value of connected porosity ϕ and its geometrical properties are of primary interest for characterizing hydrodynamic processes. *Connected porosity* is routinely measured using gas (helium or nitrogen) porosimeter. This is a fast and cheap method where the Boyle's law $(p_1V_1 = p_2V_2)$ is used to determine the porosity from pressurizing at pressure p_1 a tank of known volume V_1 containing a rock core of known total volume V_T, then opening this tank to a second tank of known volume V_2 and measuring p_2. The connected porosity is:

$$\phi = V_T^{-1}[1 - V_1 + ((p_2V_2)/(p_2 - p_1))] \tag{6.2.1}$$

Another standard method for investigating the porosity and the pore structure is *mercury intrusion porosimetry* (MIP) which provides precious information on the distribution of the pore access (Giesche 2006). This method consists of injecting mercury (i.e. a non-wetting liquid) at increasing pressure into a rock core. This corresponds to a drainage experiment (see Sect. 6.2.3). The porosity is known from the total volume injected fluid while the size of the pore access (pore throat) is inferred from the pressure p needed to force the liquid into capillaries-like throats of radius r against the surface tension force using the Young-Laplace equation $r(p) = 2\gamma \mathrm{Cos}\alpha/p$, where γ is the interfacial tension and α the contact angle between the rock and the air. MIP is an invasive method and the sample cannot be

used for other purposes after measurement, but it is a unique method for determining throat diameter ranging over five orders of magnitude from few nanometers to hundreds of micrometers.

In addition to the value of the porosity, the geometry of the pore network (pores and throats) controls the flow of single or multi-phase fluids. There are several (complementary) approaches for measuring the average geometrical properties of the pore space. The most studied ones are certainly the tortuosity factor and the specific surface.

Tortuosity is a key parameter for characterizing macroscopically flow and transport properties in rocks. There are many models for tortuosity estimation based on the underlying physical process involved. The geometrical tortuosity τ_G denotes the sample-averaged ratio of the length of the mean trajectory between two points to the lineal distance between these two points. The mean trajectory is the curve that lies at equal distance to the pore walls. Tortuosity is clearly related to the degree of connection of the pore network such as the permeability is and thus a lot of research work has been devoted to relate permeability to porosity and tortuosity (see Rashid et al. 2015 for a critical review of these models). Albeit the definition of τ_G is simple, measuring the geometrical tortuosity of porous media requires defining first the geometrical skeleton of the pore space and consequently requires 3D imaging of rock samples.

Other definitions of the tortuosity can be useful. For instance electrical tortuosity (Sect. 6.2.1) and diffusional tortuosity (Sect. 6.3.1) denote the factor needed to relate the effective diffusion (of electrical potential or a solute respectively) to the diffusion that would be measured for a porosity of 1, i.e. in the fluid phase without rock. The widely used terming of electrical and diffusional tortuosity may be confusing; generally speaking they are geometrical factors which denote the average tortuosity of the displacement of electrons or tracers respectively. In simple structures such as bundles or networks of tubes displaying smooth changes in diameter, the electrical and diffusional tortuosity factors denotes the sample-scale geometrical tortuosity of diffusion paths. However, in more complex structures such as in carbonate reservoirs or even more in tight rocks such as forming the reservoir caprocks (tight carbonates, marl and claystones) the diffusional (or electrical) tortuosity factors encompasses constrictivity effects that are usually impossible to measure independently.

6.2.1.2 Electrical Tortuosity

Electrical conductivity σ_e of a water-saturated rock of known porosity ϕ is widely used to infer tortuosity using the generalized Archie's law:

$$\sigma_o/\sigma_e = \phi^{-m} \tag{6.2.2}$$

where σ_o denotes the conductivity of the water or the brine filling the connected porosity of the rock and m is a constant that depends on the geometry of the pores.

The ratio σ_o/σ_e is called the formation factor (F) because it typifies a given reservoir formation. Values of F are generally lower than about 100 for reservoir rocks while the formation factor values of caprocks are very high and denote the complexity and the high tortuosity of the claystone, tight carbonate and marl. Rashid et al. (2015) reported values ranging from 23 to 2565 with an average value of 313.

If the rock contains a low fraction (i.e. less than around 15 %) of nonconductive phases such as oil or CO_2, the porosity (ϕ) in the Archie's law denotes the fraction of the pore saturated with the brine. Thus the electrical conductivity is a method for measuring residual oil or gas saturation but requires knowing the value of m measured at brine saturation. The exponent m, called the cementation exponent, increases as the connectedness of the pore network decreases. For reservoir rocks, the value of m ranges from 1.5 to 2.5 for sandstones but can reach values as large as 5 for carbonates (Glover 2009). While ϕ and m are characteristic properties of the rock explicitly given by Eq. 6.2, electrical conductivity measurements are habitually performed to extract the electrical tortuosity τ factor. Various models have been proposed in the literature to link the electrical tortuosity with the formation factor, e.g. $F = \tau^n/\phi$, (Clennell 1997), but the usual definition of the electrical tortuosity assumes $n = 1$ and therefore τ is explicitly obtained from the electrical conductivity measurement of the water saturated sample. Accordingly, the tortuosity τ is ubiquitously related to the porosity: $\tau = \phi^{(1-m)}$.

Electrical conductivity measurements are quite easy to implement and there is a huge amount of literature discussing the technical and methodological aspects of this technique. The fundamental step is the measure of the sample conductivity using the Ohm's law, $\sigma_e = I/(S\Delta V)(L/S)$ by imposing a difference of potential ΔV between the two edges of a sample of section S and length L and measuring the current density I. Yet, there are two main limitations. First, the presence of significant fractions of clay mineral triggers non-negligible surface conductivity (σ_s) mechanisms at the pore-rock interface. In this case Archie's law must be modified, $\sigma_e = \sigma_s + \sigma_0/F$ and it is necessary to perform the measurements at different values of σ_0 for evaluating F. The second difficulty is the possible alteration of the rock sample by the brine used for the measurements specifically in carbonates and clay-rich sandstones. In any case it is recommended to use solutions that are in thermodynamic equilibrium with the rock-forming mineral to minimize fluid-rock reactions.

It is worth noticing that there are several different types of notation for the relation between the formation factor and the porosity. For instance it is often proposed the following relationship $F = \alpha/\phi^m$, where m is the cementation factor and α is named cementation intercept, lithology factor or sometimes improperly designated as the tortuosity factor. But this approach is not valid because this would indicate that $F = \alpha$ for $\phi = 1$ or in other words that $\sigma_0 = \alpha\sigma_e$ whereas by definition $\sigma_0 = \sigma_e$ in the absence of solid.

6.2.1.3 Specific Surface

The pore-mineral interface area is a critical property of reservoir rock for modeling chemical reactions such as dissolution reactions triggered by the acidification of the brine during CO_2 storage. Knowing the geometry of the pore surface is also useful for modeling relative permeability, capillary pressure and wettability mechanisms (see Sect. 6.2.3). The gas sorption method is often used for evaluating the area of the surface of the pores connected to the sample boundaries. A given mass of inert gas is injected in a sample and the amount of gas adsorbed is measured by volumetric, mass-flux or the most often pressure methods at one or several temperatures (isotherms). The raw data are processed following the BET method (Brunauer et al. 1938) in order to extract the specific surface area, i.e. surface area per unit mass. The interface between the pore and the solid phases can be also evaluated by processing microscopic images of thin sections or X-ray 3D microtomographic images (see Sect. 6.2.1). In both cases the calculated surface area is controlled by the optical resolution of the imaging technique and a fraction of the surface roughness is not resolved while BET method probes the solid surface area with a nanometer scale resolution.

6.2.1.4 Properties Extracted from X-Ray Micro-tomography Techniques

Since a decade X-ray micro-tomography (XRMT) has become a highly regarded mean for assessing pore structure geometry. Form the 3D X-ray absorption images the first step is to produce binary images where the solid and the void phases are identified. From these binary images many parameters, such as the connected and unconnected porosity, the surface to volume ratio and the geometrical tortuosity of the connected porosity can be extracted easily (Nikolaidis and Pitas 2001). Other morphological descriptors of the pore structure such as proposed in Torquato (2002) can be implemented for measuring the distribution of some characteristic of the pore size. For instance Lu and Torquato (1993) discussed the calculation and the use the chord-length distribution and the free-path distribution functions and of their momentum for macroscopically characterizing the microstructures in relation with transport problems.

XRMT images are often used to extract the porosity skeleton (Fig. 6.1). The skeleton denotes the one-dimensional reduction, centered inside the porosity body, of the connected porosity that keeps some relevant geometrical and topological features of the pore properties (Siddiqi and Pizer 2008; Lee et al. 1994). It is a powerful tool for analyzing large microtomography images of porous media (e.g. Lindquist and Venkatarangan 1999). The skeleton can be defined in tip voxels having exactly one neighbor, regular voxels having exactly two neighbors and node voxels having more than two neighbors. Tip, regular and node voxels are usually associated with porosity dead-ends, throats and pores respectively. More generally the fraction of each of these types of skeleton voxels is an interesting indicator of

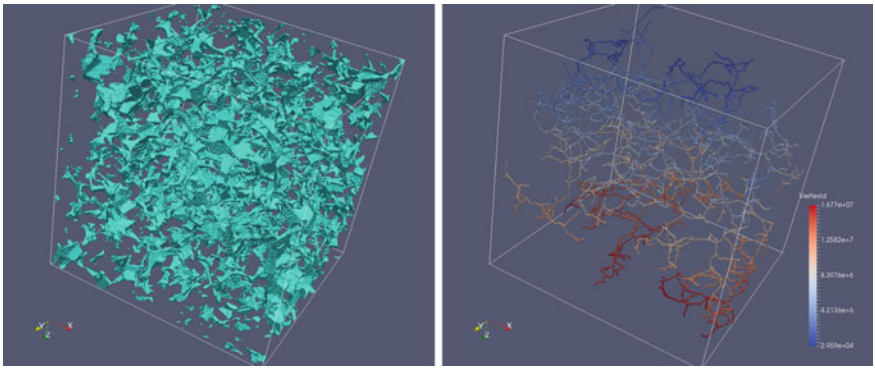

Fig. 6.1 *Left* Connected porosity of a 2563 voxel sample of Fontainebleau sandstone (voxel side size 5.06 µm) and *right* the corresponding skeleton

the overall complexity of the pore space structure. For instance, Luquot et al. (2014) used this method for identifying and characterizing the change of the porosity geometry triggered by the injection of CO_2-rich brine into reservoir rock samples. While the skeleton is obtained the radius of the largest inscribed spheres centered at each voxel forming the skeleton can be computed using for instance the Euclidean distance transform algorithm introduced by Meijster et al. (2002). This enables to derive the pore size distribution in the sample and detect the preferential flow paths.

More evolved data processing can be applied to evaluate the pore size distribution and the connectivity as well as the thermal and chemical diffusion coefficient and the diffusional tortuosity by solving the Laplace equation using for example random walk methods (Dentz et al. 2012; Sen 2004). More computation-demanding simulations, using for instance Finite Volume or Lattice Boltzmann methods (e.g. Gharbi 2014; Pan et al. 2001; Succi 2001) can be performed using the XRMT binarized images in order to calculate the permeability by solving the Navier-Stokes equation (e.g. Gharbi 2014), the hydrodynamic dispersion (e.g. Gjetvaj et al. 2015) and the elastic mechanical properties (e.g. Wojtacki et al. 2015). However, the investigated volume is inversely proportional to the complexity of the mathematical problem to be solved due to computation limitations. For example the determination of the diffusional tortuosity can be typically performed on images containing many thousands of pores, while permeability calculation is limited to sub-volumes of few hundreds of pores and mechanical properties to sub-volumes of few tens of pores. For comparison, electrical conductivity measurements, permeability measurements and mechanical tests performed in the laboratory on typical 1–2 inch diameter cores sample give properties averaged over 10^5–10^7 pores.

Moreover it is worth noticing that the representativeness of the results is highly dependent on the imaging quality and resolution and even more importantly on the accuracy of the image binarization or segmentation (e.g. Schlüter et al. 2014). Nevertheless the possibilities offered by both the imaging equipment and the numerical processing of data are continuously improved and the so called *numerical*

core analysis is now widely used, specifically because it is a non-invasive technique. Because of this remarkable advantage, XRMT can be used to monitor the changes of these properties with time in the course of dynamic experiments involving the displacement of immiscible phases or chemical rock alteration. For instance XRMT imaging has been successfully used to measure the phase saturation during imbibition and drainage experiments performed for evaluating relative permeability (Silin et al. 2011; Perrin and Benson 2010). The direct imaging of the spatial distribution of the phases (ex: CO_2 and brine) during such experiment is a powerful tool for understanding, for instance, hysteresis mechanisms or to tackle experimental bias such as induced by the finite size of the sample when performing imbibition and drainage experiments. Similarly, XRMT has been used intensively for measuring the change of porosity and other hydrodynamic properties caused by the dissolution and the precipitation of minerals linked to by the chemical disequilibrium triggered by the CO_2 injection (see Sect. 6.4).

6.2.2 Hydrodynamical Properties for Single Fluid Flow

6.2.2.1 Permeability

Intrinsic (or absolute) permeability is a fundamental property which is needed for parametrizing reservoir models. The widely use technique for determining permeability from core samples is steady state flow tests using aqueous liquids or gas. When using an incompressible liquid such as water, the fluid is injected using a constant flow rate Q [m^3 s^{-1}] through the sample and the pressure drop ΔP [Pa] between the inlet and the outlet of the sample is measured. Permeability k [m^2] is evaluated from applying Darcy's law:

$$k = (4\mu QL)/(\pi d^2 \Delta P) \tag{6.2.3}$$

where L and d denote the length and the diameter of the core sample and is μ the viscosity [Pa s]. Note that μ depends on the pressure, temperature and the composition of the fluid. Water permeability is generally an accurate method, specifically when performing the measurement for different flow rate. Doing so allows verifying that the applied flow rates are in the range where Darcy's law is valid by checking the linear relation between k and ΔP. However the use of water can trigger chemical reactions with the rock-forming mineral and consequently alter the estimated value of k (Al-Bulushi et al. 2012) and makes the measurement a destructive one. Therefore it is recommended to use water previously thermodynamically equilibrated with the rock-forming minerals. Some permeameters allows the application of axial and radial confining pressures to reproduce the mechanical constrains at depth.

Conversely, constant pressure injection while measuring the flow rate, for instance using a mass flow meter, is performed when using gas (usually nitrogen or helium). The advantages of gas permeametry are that gas does not alter the rock and the measurements are easy and fast. Nevertheless, the relation between the measured values of Q and k cannot be modeled by Darcy's law but require models that take into account the low density and the compressibility of the gas. The standard approach for processing the measured values of ΔP and Q in order to evaluate k involves the following steps (Jones and Roszelle 1978):

- Measure Q for four or five different values of the inlet and outlet gas pressures (P_{in} and P_{out});
- Evaluate the so called *gas permeability* k_G using for instance the Scheidegger's law (Wu et al. 1998; Scheidegger 1974): $k_G = (8\mu QLP_{out})/(\pi d^2(P_{in}^2 - P_{out}^2))$. The value of k_G depends on the pressure and to lesser extent to the type of gas used;
- Calculate the mean gas pressure P_{av} in the core for each measurement and plot the gas permeability against the inverse of the mean gas pressure in order to evaluate the coefficient b of the relation $k_G = k(1 + (b/P_{av}))$ that is known as the Klinkenberg's correction for the pressure-dependent slip effect of the gas at the pore-solid interface (Klinkenberg 1941). The value of the intrinsic permeability is obtained by evaluating the value of k_G at the origin: $k = k_G$ when $(1/P_{av}) \rightarrow 0$, i.e. extrapolating the measurement for an infinite pressure for which gases behave as a liquid.

The accuracy of the method depends strongly on the effective linearity of the measured values of the couple k_G and $1/P_{av}$. Often the values are very badly aligned which indicates that the law (Scheidegger's law) used to evaluate k_G is not appropriate or highlight large inaccuracy of the measurements (Bloomfield and Williams 1995). This technique can be used for rocks with permeability ranging from about 0.1 mD to 10 D.

Similar values of permeability can be measured using the so called probe-permeameter or micro-permeameter. This technique consists in measuring the pressure decay while forcing a flow of gas through a small injection tip pressed and sealed against the surface of a rock sample. By construction the method is applied to unconfined samples and the measured value may different from the value at the reservoir pressure specifically for claystones. Yet, this is a fast and simple method that can be used directly on the field to evaluate the permeability of cores (Halvorsen and Hurst 1990).

Measuring the low values of permeability of the tight rocks (i.e. permeability smaller than 0.1 mD down to about 10^{-5} mD) forming the reservoir caprocks is not a routine task. Such measurement cannot be performed using steady-state gas flow techniques because the duration required to reach steady state is too long. Non-steady-state gas flow techniques applied to cores confined at reservoir pressure can be used. The method consists in monitoring at both edge of the sample, the pressure change caused by a pressure pulse, a pressure increment or an oscillating

pressure perturbation applied at on edge of the sample using a piston pump. The permeability as well as the storativity is calculated using models that require a precise knowledge of the sample size and porosity (Metwally and Sondergeld 2011; Fischer 1992). For extremely low permeability rocks, i.e. ranging from 10^{-5} to 10^{-6} mD, transient gas flow techniques can be applied to crushed-rock and consists in monitoring the pressure decay following a pressure pulse into a closed container containing crushed-rock particles of size less than 1 mm (Cui et al. 2009).

6.2.2.2 Diffusivity

Diffusion is a ubiquitous mechanism. Mass transfer by diffusion is the dominant process in low permeability materials such as claystones and cements, but is also essential in reservoir where advection is very low (i.e. for low value of the Peclet number, see Sect. 6.4.1), for instance far from the injection well.

The effective diffusion coefficient or diffusivity coefficient is routinely measured at laboratory scale using specific diffusion cell, such as displayed in Fig. 6.2a, where the rock sample is sandwiched between two reservoirs, one of them containing the solute tracer while the other one contains tracer-free water (Tinker 1969). As diffusion is a slow process, the thickness of sample is usually small (few centimeters) in order to make the measurement tractable. Even though, diffusion measurement in tight rocks requires monitoring the tracer concentration for several tens of days. Whereas the principle is simple its set up is not straightforward specifically for permeable media (reservoir rocks) for which avoiding advection due to pressure gradient or buoyancy effects is challenging. Measuring the effective diffusion in claystone or other tight rocks displaying very low pore size porosity requires some great care as well. For instance, tracer molecule or ion of different sizes can probe different portions of the porosity and ion exclusion phenomenon

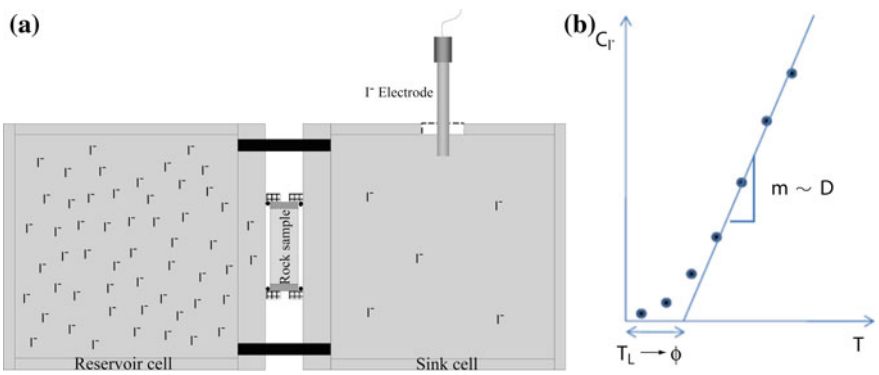

Fig. 6.2 **a** Diffusion cell apparatus for steady-state diffusion measurement. **b** Concentration versus time in the outlet reservoir displaying the linear increase of concentration occurring when the mass flux of tracer is steady state

can occurs. For example, such a phenomenon prevents chlorine and iodine anion from having access to the same porosity as a water tracer like tritiated water (HTO) or deuterium oxide (HDO). Furthermore, the intensity of the exclusion mechanism usually depends on the ionic strength of the water saturating the pores (Van Loon et al. 2003).

The simple way for measuring the breakthrough curve in the outlet reservoir is to install electrodes that measure cation or anion concentration. Nevertheless, the use of specific tracers (e.g. organic or radioactive) or mixture of tracer may exclude the use of an in situ monitoring probe and therefore implies sampling the outlet reservoir fluid. The calculation of the effective diffusion coefficient D_e is based on Fick's second law assuming one-dimensional transport geometry:

$$\phi \frac{\partial C}{\partial t} = D_e \frac{\partial^2 C}{\partial x^2} \tag{6.2.4}$$

where C is the tracer concentration [mol m^{-3}], t the time [s] and D_e the effective diffusion coefficient [m^2 s^{-1}]. Usually the measurements are performed with the initial condition $C(0 \leq x \leq L, t = 0) = 0$, where L denotes the sample of length.

Using reservoirs of large volume allows assuming that there is a finite interval of time during which the concentration boundary can be considered as constant $C(x = 0, t > 0) = C_i$ with C_i the initial tracer concentration in the inlet reservoir and $C(x = L, t > 0) = 0$ if there is no tracer in the outlet reservoir initially, while the flux of tracer Φ is constant $\Phi = -D_e \partial C/\partial x = D_e C_i/L$ (Crank 1975; van Brakel and Heertjes 1974). For this period of time, the concentration of tracer in the outlet reservoir, C_o, increases linearly with time $C_o(t) = D_e C_i S t/V_o L$ (Fig. 6.2b), where V_o denotes the outlet reservoir volume and S the surface of the sample in contact with the reservoir. Accordingly, the effective diffusion coefficient is given by:

$$D_e = \frac{V_o L}{C_i S} \frac{\partial C_o(t)}{\partial t} \tag{6.2.5}$$

Analytical solutions of the complete transient diffusion problem (Eq. 6.2.4), including the change of concentration in the reservoir and the change in the reservoir volume if samplings are performed, can be obtained in the Laplace domain and then numerically inversed in order to be fitted to the experimental data. In this case both the porosity and the effective diffusion coefficient can be evaluated. Also it is worth noticing that the formal equivalence between the Fick's law and the Ohm's law (Sect. 6.2.1) allows the evaluation of the value of D_e from knowledge of the electrical tortuosity: $D_e = \phi D_0/\tau$, where D_0 denotes the molecular diffusion of the tracer in water (e.g. Garrouch et al. 2001).

6.2.2.3 Dispersion

Evaluating the coefficient of dispersion of the Fickian advection-dispersion equation (see Chap. 3) is not straight forward because this coefficient is strongly dependent on the measurement scale. Considering samples of characteristic size and time the tracer need to cross a rock sample of few centimeters long for usual flow rates (<1 md^{-1}), the asymptotic dispersion is usually not reached and therefore is not possible to determine the Fickian dispersion coefficient (Gjetvaj et al. 2015; Cortis and Berkowitz 2004; Levy and Berkowitz 2003; Berkowitz et al. 2000). Still, dispersion mechanisms can be studied by performing tracer tests that are similar to those used for diffusivity (Sect. 6.2.2) but applying a constant flow rate at one edge of the sample. While the steady state flow in sample is reached, a pulse of tracer is injected as close as possible to the sample inlet. The main technical issues are (i) the injection of a pulse of tracer of very short duration while minimizing the flow perturbation, (ii) avoiding spurious dispersion before the tracer enter the sample and (iii) assuring a homogeneous concentration at the sample inlet surface. Thus the volume of the traced fluid to be injected must be small and the concentration of the tracer sufficiently high to allows the measurement of the effluent tracer concentration over, at least, 3 orders of magnitude in concentration, but sufficiently low to avoid density effects (Tenchine and Gouze 2005). Furthermore, the tracer must not interact with the rock-forming minerals, i.e. avoiding sorption and chemical reactions such as dissolution and precipitation. For these reasons fluorescent dies are often used because their low reactivity and because optical techniques using high sensitivity sensors allows measuring a large range of tracer concentration values down to values as low as 10^{-10} mol of tracer per mole of water.

There are two methods to perform tracer tests. The standard method, named flow-through tracer test, consists in injecting the tracer at one side of the core and measure the breakthrough curve at the opposite side of the core. However, it can be useful to perform push-pull experiments in order to better characterize the long-time behavior of the dispersion mechanisms and compare the reversible part of the dispersion due to the hydrodynamic spreading of the tracer to the irreversible part of the tracer dispersion triggered by diffusion (Gouze et al. 2008).

The equipment displayed in Fig. 6.3 is designed to allow both flow-through and push-pull experiments without any change in the circuit when changing experiment type. Water is pumped into the circuit with two piston pumps, passes through tracer injection point, sample core and out of the system. Arrows indicate the direction of flow for different experiment stages. Blue arrows indicate flow direction in the branches of the circuit where flow direction is always the same, green arrows indicate flow direction during a flow-through experiment and during the pull phase of push-pull experiment, while red arrows indicate flow direction during push phase of push-pull experiment. The TELOG sensor (ICARE Lab. Montpellier) is a high resolution optical for measuring fluorescent dye implementing pulsed light sources and a high sensitivity photomultiplier for measuring tracer concentration from 10^{-6} to 10^{-10} mol of tracer per mole of water.

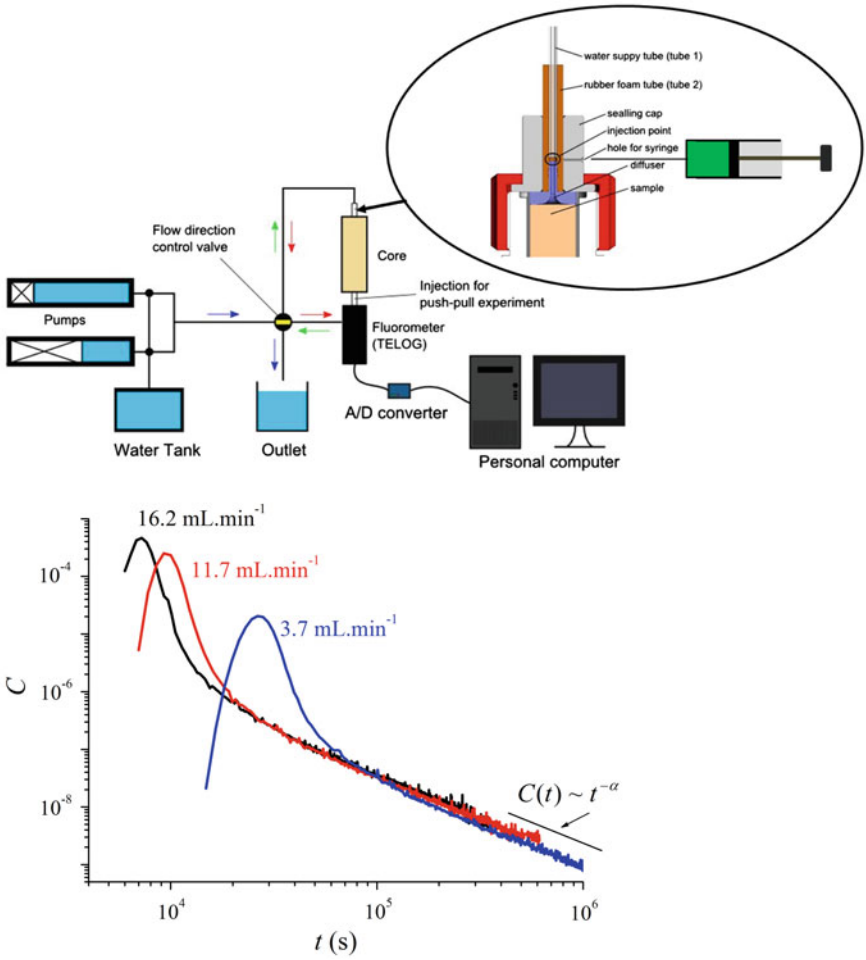

Fig. 6.3 *Top* Schematic diagram of the tracer test equipment layout with arrows indicating flow direction. *Blue arrows*-permanent flow direction; *green arrows*-flow direction for flow through experiments and the-pull phase of push-pull experiments; *red arrows*-flow direction during the push phase of push-pull experiments. *Bottom* Example of breakthrough curves (concentration versus time) measured during a passive tracer dispersion experiments in carbonate cores of diameter 90 mm and length 557 mm for different flow rates. Details of the experiments are given in Gouze et al. (2009)

For flow-through experiment configuration the water arrives at the top of the sample. The given volume of tracer is injected with a micro syringe to precisely dose the tracer volume and control the duration of the injection. Then, the solute passes through the sample and the outlet concentration is measured by the TELOG sensor. For the *push* phase of a push-pull experiment, flow direction valve is placed in position to direct flow at the bottom of cell. There is another injection point just

between the TELOG and sample. Tracer is push for a period of time depending on flow rate, permeability and length of sample in order to investigate as much as possible of the porous media without any tracer leaving from the sample at the other side. At the end of push period the control valve is switched and the water starts to flow from the top of the sample like during flow through experiment. In order to emphasize dispersion due to diffusion a resting time (no flow) between the push phase and the pull phase can be done.

Usually, the measured breakthrough curves (BTC), i.e. the tracer concentration in the effluent versus time, display strongly asymmetric shapes with long tails (i.e., for times larger than the time corresponding to the advective peak arrival t_a) that appears to decrease more or less as a power law of time $C(t \gg t_a) \sim t^{-\beta}$, and indicates an apparently infinite variance. These are characteristics of non Fickian dispersion and the interpretation of these data must be done in the framework of non-Fickian models. Non-Fickian dispersion properties, their origin and their relation to the geological heterogeneity are the source of debates. Authors have explored different approaches for better modeling pre-asymptotic processes that result from (long-range) spatial correlation of geological structures and consequently of fluid velocities. Often these models leads to non-local in time transport equations that are solved using random walk approaches such as Continuous Time Random Walk (Berkowitz et al. 2000) or Time Domain Random Walk (Russian et al. 2016). The results of dispersion experiments are useful for parametrizing the models presented in Chap. 5, such as based on the Multirate Mass Transfer, Continuous Time Random Walk or Fractional Advection-Dispersion Equations approaches.

6.2.3 Measuring Capillary Pressure and Relative Permeability for scCO$_2$-Brine Systems

The objective of this section is to present the methods for measuring the relative permeability versus saturation data that are required for applying the extended or generalized Darcy law to biphasic flow (see Chap. 3 and Sect. 5.5). Two and three non-miscible phases flow in porous rocks involves complex mechanisms (e.g. Sahimi 2011) and thus measuring relative permeability requires demanding laboratory and data processing works.

In the following we will assume that the porosity of rock is saturated with a mixture of two immiscible fluids: CO_2 and brine. The relative permeability $k_i^{(r)}(S_i)$ is a dimensionless measure of the effective permeability of phase i ($i = C$ for CO_2 or b for brine) for a saturation (S_i) and is defined as $k_i^{(r)}(S_i) = k_i^{(e)}(S_i)/k^*$ where $k_i^{(e)}(S_i)$ denotes the effective permeability of phase i and k^* the reference permeability (in m^2). The choice of reference permeability is not critical as soon as it is consistent with the model in which the values of $k_i^{(r)}$ will be implemented, but often

the intrinsic permeability is used or alternatively the CO_2 permeability measured at irreducible brine saturation. Similarly, relative permeability of CO_2 and brine are usually expressed as the function of the brine saturation $k_i^{(r)}(S_b)$.

The (relative) displacement of CO_2 or brine is controlled by a range of physical and chemical factors that yield viscous forces and capillary forces. Their respective control on the hydrodynamics of the fluid pair is scaled by the capillary number $Ca = \mu v/\sigma$, where μ, v and σ denote the average dynamic viscosity [Pa s], the average fluid velocity [m s^{-1}] and the surface or interfacial tension between the two fluid phases in [N m^{-1} or Pa m]. Usually, capillary forces dominate in natural reservoir flow (Hilfer and Øren 1996; $Ca < 10^{-8}$). However, in the vicinity of the injection well the value of Ca increases as v increases.

6.2.3.1 Wettability and Capillary Pressure

Capillary forces arise from the interactions between the fluid pair and the rock-forming minerals in contact with the fluids. When two fluid phases are present, the wettability denotes the contact angle θ_{fs} of the fluid f with the solid phase s. Wettability results from surface tension due to attractive forces between the fluid molecules and the solid surface while cohesive forces takes place within each of the fluid phase and create an interfacial tension σ. If $\theta_{fs} < 90°$ for a given fluid phase and a given solid phase, then this fluid preferentially covers the solid phase and it is named the wetting fluid. Like for interfacial tension, wettability depends on pressure and temperature. Under typical reservoir conditions most of the rock-forming minerals such as quartz, feldspar, calcite, dolomite and clay minerals are brine wet and the CO_2 as a gas or a supercritical phase is the non-wetting fluid. Examples of CO_2 wettability values for reservoir and seal rocks as well as discussions of the potential wettability alteration due to the flushing of rocks by CO_2 are given in Iglauer et al. (2015), Chiquet et al. (2007), Zhu et al. (2011) and Wang et al. (2012).

When one of the fluid pair displaces the other one, capillary forces triggers differential pressure between them that is named the capillary pressure P_c (in Pa). P_c is defined as the pressure difference between the non-wetting phase and the wetting phase. At equilibrium, i.e. without any external forces such as an advective fluid flow, the Young–Laplace equation gives the capillary pressure as the function of the interfacial tension σ, the wetting angle θ of the brine on the surface of the capillary and the curvature radii of the respective fluids. In a capillary of the radius r the Young–Laplace equation is written $P_c = (2\sigma \mathrm{Cos}\theta_{fs})/r$. These parameters are defined at pore scale, but macroscopic equivalent values are needed for describing multiphase flow in porous media. At macroscopic scale P_c is primarily controlled by the extension of the interface area between the fluid pair and the solid and thus depends on both the fraction of each of the phase saturating the pore space and the porosity topology. Evidently pores in rocks are not capillary-shaped and pore and throat diameters are (highly) variable. From the seminal works of Leverett (1941) and Bear (1972) there have been many different derivations of the capillary pressure

in porous media using geometrical and, or, thermodynamic considerations (see for example Hassanizadeh and Gray 1993). These model are useful for instance to evaluate the pore size distribution from capillary pressure measurements such as mentioned in Sect. 6.2.1.

Sample scale capillary pressure curves are typically measured by performing drainage experiments which consists in forcing the displacement of a wetting fluid by a non-wetting fluid, using centrifuge methods or mercury (Hg) injection porosimetry (MIP). For the later, the pressure needed to inject Hg in the vacuumed sample gives the Hg/air capillary pressure $P_c^{(Hg/a)}$ versus the (cumulative) volume of Hg injected at room temperature. These data can be extrapolated to CO_2/brine capillary pressure $P_c^{(C/b)}$ at relevant temperature (and pressure) using the relation given by Washburn (1921):

$$\frac{P_c^{(C/b)}}{P_c^{(Hg/a)}} = \frac{\sigma^{(C/b)} \cos\theta^{(C/b)}}{\sigma^{(Hg/a)} \cos\theta^{(Hg/a)}} \tag{6.2.6}$$

The values of the interfacial tension can be found in the literature for the given fluid, pressure and temperature ($\sigma^{(C/b)} \cong 3 \times 10^{-2}$ N m^{-1} in reservoir conditions and $\sigma^{(Hg/a)} \cong 0.5$ N m^{-1} at room temperature; e.g. Georgiadis et al. 2010), but values of the contact angle for the system CO_2/brine/rock under consideration are often not known and usually it is assumed that $\theta^{(C/b)} = \theta^{(Hg/a)}$ (Hingerl et al. 2016; Krevor et al. 2012; Pentland et al. 2011). The capillary pressure$P_c^{(C/b)}$ versus brine saturation S_b data are commonly fitted using the Brooks-Corey model (Brooks and Corey 1964):

$$P_c^{(C/b)} = P_{\min}^{(C/b)} \left(\frac{1 - S_b^{(0)}}{S_b - S_b^{(0)}} \right)^{1/A} \tag{6.2.7}$$

where $P_{\min}^{(C/b)}$, S_b and $S_b^{(0)}$ denote the minimum pressure needed for the CO_2 to penetrate the sample, the actual brine saturation and the residual brine saturation, respectively. $S_b^{(0)}$ is also often termed critical brine saturation or irreducible brine saturation, and denotes the maximum brine saturation at which the brine remains immobile while the sample is flushed with CO_2. In Eq. 6.2.7 A is a fitting (positive) parameter named the pore size distribution index. $P_{\min}^{(C/b)}$ can be regarded as a fitting parameter or can be evaluated from drainage experiment such as described below. Note that Eq. 6.2.7 denotes a simple monotonic decreasing function $P_c^{(C/b)}(S_b)$ and consequently it is sometimes impossible to fit experimental data with the Brooks-Corey equation (e.g. see an example in Krevor et al. 2012).

Drainage experiments using brine and CO_2, as well as imbibition experiments (flushing CO_2 with brine) can be performed in order to measure the $P_c^{(C/b)}$ versus

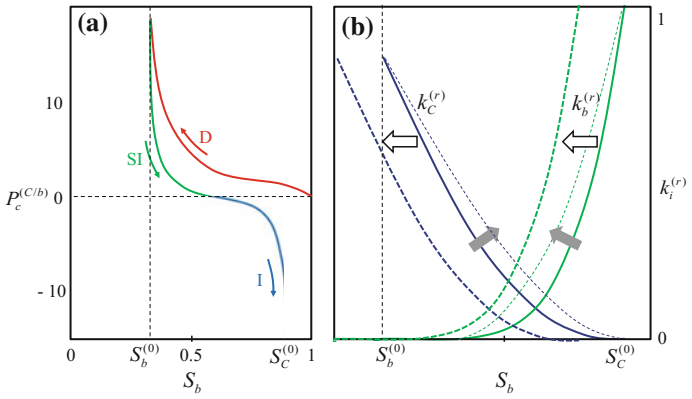

Fig. 6.4 **a** Schematic representation of capillary pressure versus brine saturation. Label D, SI and I denotes the forced drainage, spontaneous imbibition and forced imbibition stage respectively. **b** Schematic representation of relative permeability curves for CO_2 and brine versus brine saturation for a given value of the capillary number and wettability. *Plain arrows* indicate the expected change of the shape of relative permeability curves when the value of the capillary number increases. Lower wettability will tend to shift the curves toward lower values of the brine saturation

S_b. These experiments are also used to measure relative permeability $k_i^{(r)}$ versus S_i ($i = CO_2$ or brine) as it will be explained in the next section (Sect. 6.2.3). Figure 6.4a displays a typical capillary pressure curve $P_c^{(C/b)}$ versus S_b. Starting from fully brine saturated rock sample, the primary process (noted D) is the forced drainage of the brine by the CO_2 which ends when only residual brine saturation $S_b^{(0)}$ is reached and gives the maximum capillary pressure. The second stage (noted SI) displays the spontaneous imbibition where the brine invades the rock due to capillary forces until $P_c^{(C/b)} = 0$, then the third process (noted I) is the forced imbibition for which the brine displaces the CO_2. Eventually the brine saturation reaches an asymptotic value corresponding to the residual CO_2 saturation $S_C^{(0)}$.

6.2.3.2 Experimental Evaluation of the CO_2 and Brine Relative Permeability

Several methods have been proposed for the calculation of relative permeability from capillary pressure data, stating from the seminal works of Purcell (1949), then discussed for instance in Li and Horne (2002). Most of these models relate directly on the evaluation of the pore size distribution derived that can be derived from MIP (Brooks and Corey 1966) or centrifuge experiments (Pinter and Bodi 2012). The calculation of relative permeability from capillary pressure versus saturation data have been largely used to unsaturated flow of water in soil applications using

models relating capillary pressure to saturation such as proposed by Brooks and Corey (1964), Durner (1994), Kosugi (1996), Seki (2007) and van Genuchten (1980). Applications to the flow of oil and brine in reservoir rocks are discussed in Honarpour et al. (1986) and a review of these methods can be found in Li and Horne (2006). The *op. cit.* authors concluded that these methods give acceptable results for drainage but are less accurate for imbibition.

Specific experiments using the brine and CO_2 at pressure and temperature of the targeted reservoir are often preferred to extrapolations from mercury injection or centrifuge methods using brine and air at room conditions. The basic procedure for measuring relative permeability is to perform imbibition (displacing CO_2 with brine) and drainage (displacing brine with CO_2) experiments or injecting mixture of CO_2 and brine into a rock sample. The effective permeability must be measured over the largest-as-possible range of fluid saturations in order to construct the relative permeability curves. Fluid displacement experiments, i.e. drainage or imbibition performed at different intrusion pressure, are named transient methods (Berg et al. 2013; Johnson et al. 1959) while simultaneous injection of the two phases at given fractions are named steady state flow methods (Virnovsky et al. 1995; Dake 1978).

As already mentioned, the transient flow of two immiscible fluids depends on the sample-scale capillary pressure (and consequently on the geometry of the pore network), on the wettability of the fluids for this given rock sample, and on the interfacial tension between the CO_2 and the brine. These complex mechanisms together with the thermodynamic properties of the fluids hinder the measurement procedure. Hereafter are listed some major issues related to the experimental appraisal of relative permeability. Wettability depends on the brine composition (e.g. some solute components can act as surfactants) and furthermore both wettability and interfacial tension depend on temperature (e.g. Hamouda et al. 2008). Thus, it is recommended to perform the measurements at temperature close to that of the reservoir using brine of composition corresponding to the thermodynamically equilibrated reservoir brine. For CO_2 underground storage applications, the CO_2 is in supercritical state and furthermore the brine and the CO_2 must be thermodynamically equilibrated under experimental pressure and temperature conditions prior to be pumped into the sample in order to avoid drying of the residual brine saturation, specifically for drainage experiments. This implies that a fraction of CO_2 dissolves in the brine and creates an acidic fluid that can promote the dissolution of minerals such as carbonates (see Sect. 6.4.4). Also, relative permeability experiments usually start from cleaned cores and a specific attention must be played to the cleaning protocol which may alter the wettability of the surface of some minerals. Furthermore, capillary effects occurring at the sample edges where the fluid(s) are injected and produced can hamper the measurement if not treated properly using adapted experimental techniques and data processing (Huang and Honarpour 1998). These mechanisms are named capillary end-effects and can be the source of high uncertainty in the results if not recognized and corrected appropriately. Finally it is important to mention that hysteresis mechanisms triggered by the existence of residual phase fraction and multiple metastable configurations of the (pore-scale)

distribution of the phases depending on the saturation history (Cueto-Felgueroso and Juanes 2016; Moebius and Or 2012; Morrow 1970; Haines 1930) may require performing both drainage and imbibition measurements at different flow rates (e.g. Pini and Benson 2013). Finally, it is recommended to apply a differential pressure much smaller than the average operating pressure in order to minimize errors on the volume calculations of the CO_2 which is a compressible fluid at the pressure and temperature of the reservoirs. All together these different issues make the measurement of relative permeability challenging and induce the use sophisticated equipment, experimental protocols and data processing. Therefore, the procedures are noticeably variable from one research center to another with specific technical and theoretical adaptations to improve the measurement accuracy for the different types of rocks and reservoir conditions. For example the multiple-core method known also as the Penn State method, consists in sandwiching the rock sample with two other rock samples to reduce capillary end-effects at the inlet and outlet of the central sample during steady state experiments where two fluid phases are pumped through the sample at constant flow rates. In any case, relative permeability experiments are time-consuming, e.g. from several hours for high permeability rocks to weeks for the low permeability rocks.

The unsteady state method inherits from capillary pressure measurements and is the most used method for measuring relative permeability because it is usually noticeably faster than the steady state method. For CO_2 storage applications the optimal experimental protocol includes a drainage stage followed by an imbibition stage. The core sample is initially saturated with brine under vacuum, then brine is injected at different pressure in order to measure the intrinsic permeability k using Darcy law. Subsequently, CO_2 is pumped at constant flow rate or at constant pressure while the pressure drop across the sample or the total flow rate as well as the fraction of CO_2 and brine produced are monitored. Note that applying constant pressure minimizes the source of error due to the compressibility of the CO_2 phase. CO_2 is injected until the fraction of brine produced at the sample outlet is zero and allows evaluating $S_b^{(0)}$ the residual brine saturation and $k_C^e(S_b^{(0)})$ the effective permeability of CO_2 at the residual brine saturation. Then a similar procedure is applied but with the injection of the brine. When the fraction of CO_2 produced at the outlet reach zero one obtains the value of the permeability of the brine at the residual CO_2 saturation $k_C^{(e)}(S_b^{(0)})$. The residual saturation of CO_2, $S_b^{(0)}$ is an important parameter because pore scale residual trapping of CO_2 (as micrometer-sized bubbles hold by capillary forces in the rock pores) is a key mechanism for prevents the CO_2 from leaking back to the surface.

The value of the flow rate must be set according to the objective of the study. For CO_2 storage application it is important to obtain relative permeability curves for conditions corresponding to low value of Ca in order to model the hydrodynamics of the reservoir far from the injection location (usually $Ca < 10^{-8}$). However high flow rates are usually preferred for minimizing the impact of capillary end-effects that may take place at the sample edges that are in contact with the single phase fluid. Yet high flow rate may trigger the displacement of fine particles that may be

present into the pores and consequently compromise the measurement. To determine the appropriate flow rate it is recommended to perform few preliminary experiments at increasing values of the flow rate in order to determine when capillary end-effects are negligible while keeping in the range of value that are representative of the targeted reservoir. Together with the complexity of the data processing that will be discussed below, the main disadvantage of unsteady state methods, where a fluid displaces another fluid of distinctly different thermodynamic properties, is that this configuration can promote flow localization (fingering) mechanisms caused by the interplay of gravity and viscosity segregation effects and the porosity heterogeneities. Thus, the phase with the higher mobility (i.e. the CO_2) may bypass regions of low permeability. In this case the measured relative permeability will not be representative of the entire sample (Chang et al. 1997) and furthermore not representative of the reservoir because these localization mechanisms are also amplified by the finite-size nature of the sample.

In the course of drainage-imbibition experiments capillary pressure in the sample is space and time distributed and there are several methods (often named data reduction methods) used to process the experimentally measured time-resolved data (i.e. the flow rate, the cumulative injected volume, the phase fraction produced and the pressure drop ΔP) and evaluate the effective and relative permeability values versus saturation. For high flow rate experiments the most used processing methods are those proposed by Welge (1952), Johnson et al. (1959) and Jones and Roszelle (1978). These methods are built from assumption-based simplifications of the Buckley-Leverett model of two phases displacement; the main assumption being to neglect capillary pressure effects. Eliminating inaccuracies caused by the capillary end-effect, specifically for low flow rate experiments, has been investigated by several authors (e.g. Ramakrishnan and Cappiello 1991; Virnovsky et al. 1995). As a general description, these methods need an evaluation the phase saturation at the edge of the sample using empirical relationships requiring the calculation of the fractional flow that is defined as the derivative of the produced flow rate of the drained phase by the flow rate of the injected phase. Then the relative permeability is expressed as the function of fractional flow, the viscosity and other model-specific parameters through iterative (or history matching) methods using trial-and-error simulations (e.g. Zhang et al. 2012). The derivation of these different models is complex and several softwares and graphical methods have been developed to assist the processing of the experimental data, most of them being specifically adapted to a given experimental protocol developed by a given research center. While unsteady state method is fast relative to the steady sate method, it is often practically impossible to perform measurement for the low end of the brine saturation values.

Conversely, the steady state method requires more complex equipment and more importantly involves longer experimental durations, but allows simple data processing and often produce more reproducible and potentially accurate results. The principle of the steady state method is to measure the effective or relative permeability of the two fluids at different saturation values when the capillary pressure along the sample is negligible, i.e. the fraction CO_2 and brine is the same along the

sample. The duration of the experiment is typically ten times longer than for the high flow rate unsteady state experiments and makes this method restricted to high permeability rocks. The first steps of the experiment are similar to those described for the unsteady state method for drainage: the core sample is saturated with brine under vacuum, and then brine is injected to measure the intrinsic permeability k. Next, brine and CO_2 are co-injected starting from low value of the CO_2/brine ratio. It is usually required to pump a volume of mixture corresponding to 4–6 times the sample pore volume before steady state is reached, i.e. when the phase fraction of the produced mixture and the pressure drop are constant. This procedure is repeated for increasing the CO_2/brine ratio until 100 % CO_2 is injected and the value of the residual brine saturation and the permeability of the CO_2 at residual brine saturation $k_C^{(e)}(S_b^{(0)})$ are measured. Note that some rocks displays fast growing capillary pressure when the brine saturation decreases and thus it is difficult to avoid saturation gradient along the sample when injecting the highest CO_2/brine ratios because high pressure is needed to overpass the high interfacial tension between CO_2 and brine and the low viscosity of the CO_2; this is an open issue discussed for instance in Levine et al. (2014), Pini and Benson (2013) and Krevor et al. (2012). The same procedure can be repeated but with decreasing the CO_2/brine ratio to simulate an imbibition process, until 100 % brine is injected and the value of the residual CO_2 saturation and the permeability of the brine at residual CO_2 saturation $k_C^{(e)}(S_b^{(0)})$ are measured.

Albeit the difficulties of measuring the relative permeability of CO_2 at residual brine saturation mentioned above, the processing of the experimental data is quite simple because of the steady state nature of the biphasic flow in the rock. Indeed at steady state the saturation of each phase and the capillary pressure are constant along the core and the pressure drop for each of the phase equal the total pressure drop ΔP. Thus, the relative permeability of phase i ($i = CO_2$ or brine) at each saturation stage is given by the generalized Darcy's law: $k_i^{(r)} \cong (\mu_i L Q_i)/(kA\Delta P)$ where L and A are the length and the edges surface of the sample and μ_i and integration of the heterogeneityQ_i denotes the viscosity and the flow rate (in $m^3\ s^{-1}$) of the phase i. Capillary end effects steady state methods can be as significant as for the unsteady state method, (Kamath et al. 1995), but can be handled using adequate experimental protocol such as proposed by Pini and Benson (2013). Some results comparison between these two methods for CO_2-brine systems are given in Mathias et al. (2013) and Burnside and Naylor (2014). Figure 6.4b displays a typical relative permeability curve $k_i^{(r)}$ versus S_b where the effects of capillary number Ca and wettability are outlined.

For both steady and unsteady state methods, X-ray attenuation can be used to determine the distribution of the phase within the core sample. Usually X-ray absorbents, such as NaBr, are added to the brine to increase the contrast between the phases. It is specifically useful for verifying that no gradient of saturation exits along the sample for steady state experiments and for determining the amplitude of the capillary pressure end-effects (Berg et al. 2013). Imagery methods are

specifically helpful for obtaining relative permeability data in low-permeability rocks (Zhang et al. 2014) where the effect of capillary pressure are dominant due to tightness of the pores and throats and the capillary end-effect significant (Akin and Kovscek 1999). X-ray tomography, which allows a 3D characterization of the phase distribution, is also a very promising technique to help processing both the unsteady state and the steady state permeability experiments, giving crucial information on the displacement of the front and properties of the interfaces between the phases, but also to study the CO_2 trapping mechanisms as the function of the properties of the pore network (Andrew et al. 2014; Hingerl et al. 2016; Iglauer et al. 2011; Krevor et al. 2012; Rahman et al. 2016).

Once the experimental values of CO_2 and brine relative permeability versus brine saturation are obtained, heuristic models are usually employed to interpret the relative permeability curves and extrapolate them to brine saturation values not achievable experimentally. Several models have been proposed starting from the simple formulation proposed by Corey (1954) where the two fitting parameters are the exponents n and m of the following power law equations:

$$k_b^{(r)} = k_b^{(0)} \left[S_b^*\right]^n \tag{6.2.8}$$

and

$$k_C^{(r)} = k_C^{(0)} \left[1 - S_b^*\right]^m \tag{6.2.9}$$

with S_b^* is the normalized water saturation defined as

$$S_b^* = \left(S_b - S_b^{(0)}\right) / \left(1 - S_b^{(0)} - S_C^{(0)}\right) \tag{6.2.10}$$

Other models with higher degree of freedom are often required to model the data. For examples the exponential models proposed by Chierici (1984) involves two fitting parameters per phase while the more recent LET model (Lomeland et al. 2005; Ebeltoft et al. 2014) involves three fitting parameters per phase (I_i, L_i and E_i):

$$k_b^{(r)} = \frac{k_b^{(0)} \left[S_b^*\right]^{L_b}}{\left[S_b^*\right]^{L_b} + E_b \left[1 - S_b^*\right]^{T_b}} \tag{6.2.11}$$

$$k_C^{(r)} = \frac{k_C^{(0)} \left[1 - S_b^*\right]^{L_C}}{\left[1 - S_b^*\right]^{L_C} + E_b \left[S_b^*\right]^{T_C}} \tag{6.2.12}$$

A comparative analysis of the performance and associated uncertainty of these models using steady state relative permeability measurements can be found in Moghadasi et al. (2015).

6.3 Experiments for Solid Matrix Mechanical Properties

This section summaries state-of-the-art experimental techniques for solid matrix mechanical testing, followed by a discussion on implications and remaining issues for mechanical properties within the context of CO_2 storage. The experimental equipment and conventional methods to determine static elastic moduli, dynamic elastic moduli and strength parameters will be only briefly outlined as they have been described in several publications (e.g. Jaeger et al. 2007) and used for decades.

Experimental measurements of rock mechanical properties determine the elastic moduli and strength parameters. The elastic moduli define the rocks ability to resist and recover from deformations produced by applied stress. These are primarily represented by the modulus of elasticity (E) which is a measure of the stiffness of the sample, i.e. the samples resistance against being compressed by a uniaxial stress and Poisson's ratio (v) which is a measure of the lateral expansion relative to longitudinal contraction. The strength parameters define the rocks resistance to deformation, defining how well cemented the rock is. They are primarily represented by the uniaxial compressive strength, triaxial stress factor, cohesion and angle of internal friction. The uniaxial compressive strength (Co) is the maximum stress the rock sample can withstand. If shear failure occurs the greatest shearing stress always occurs on the planes that contain the σ_2 axis which means in practice fractures generally form at an angle between 45° and 30° to the principal axes. With reference to Mohr-Coulombs work, the shearing stress can be related to the concept of internal friction, which suggests that at failure the relationship between the magnitude of shear stress (τ) and normal stress (σ_n) is:

$$|\tau| = So + \mu\sigma_n| \tag{6.3.1}$$

where So is the inherent shear stress of the rock, termed cohesion and μ is the coefficient of internal friction. The angle of internal friction (φ) is related to the coefficient of internal friction μ by:

$$\mathrm{Tan}\,\varphi = \mu \tag{6.3.2}$$

The triaxial stress factor (k) is expressed in terms of the principal stresses (σ_1 and σ_3) which generated the normal and shear stresses (σ_n and τ) at failure and is directly related to the angle of internal friction (φ) by:

$$k = (1 + \mathrm{Sin}\,\varphi)/(1 - \mathrm{Sin}\,\varphi) \tag{6.3.3}$$

The same basic test facility is used for both elastic deformation and strength parameter determination. The samples are loaded into a pressure vessel and axial stress is transferred to the ends of the rock sample via hardened steel platens within a pressure vessel held within a servo controlled stiff testing machine. Radial stress (confining pressure) is transmitted to the rock sample via oil retained in the annular space between a rubber sleeve surrounding the sample and the body of the pressure

vessel and applied through hydraulic fluids generated by a servo controlled pressure intensifier. Strain gauges applied to the surface of the rock sample allow axial and radial strain changes during testing to be recorded. For conventional rock mechanical testing the Hoek-Franklin triaxial cell is used which allows a stress state of $\sigma_1 > \sigma_2 = \sigma_3$ to be realized (Hoek and Franklin 1968). The true in-situ stress state of $\sigma_1 > \sigma_2 > \sigma_3$ cannot be achieved in a Hoek cell, however the true triaxial pressure vessel, (Smart et al. 1999) has an array of 24 trapped tubes where selective pressurisation of the tubes enables differential radial stresses to be generated, while axial stresses are applied as conventionally, through steel plates.

6.3.1 Static Elastic Moduli Testing

Samples are loaded hydrostatically (the axial and radial confining stress are the same) in increasing increments, once each hydrostatic stress level is reached the axial stress is increased and decreased by approximately 3 kN to induce vertical and horizontal strain. The axial (σ_a) and radial (σ_r) strains are measured by the strain gauges. The modulus of elasticity (E), is calculated as the ratio of the change in axial stress (σ_a) to the change in axial strain (ε_a) and Poisson's ratio (v) is calculated from the ratio of the accompanying change in radial strain (ε_r) to the change in axial strain (ε_a).

The velocity of elastic waves in a rock is a function of its density and elasticity, therefore the mechanical parameters of modulus of elasticity (E), Poisson's ratio (v), shear modulus (G), bulk modulus (K) and compressibility (Cb) can also be determined if the bulk density (ρ_b) of the rock is known. Elastic properties derived from acoustic measurements are known as dynamic elastic moduli. There is a wide range of experimental evidences to show that static and dynamic moduli of rocks are different, (Fjar et al. 1992). In general the static elastic modulus for dry rocks is less that the dynamic modulus. The most common reason for the described is ascribed to the presence of microcracks.

6.3.2 Strength Parameter Testing

A basic compressive strength test involves loading a sample to failure at a constant value of confining pressure. This results in a single pair of maximum and minimum principle stresses and the determination of stress at failure, i.e. the uniaxial compressive strength. This straightforward test does not facilitate the determination of any other strength parameters which require the construction of a Mohr's failure envelope, generated from several Mohr's circles determined on the same sample at different confining pressures. The uniaxial compressive strength (UCS) can be calculated by dividing the load at failure by the cross sectional area of the sample.

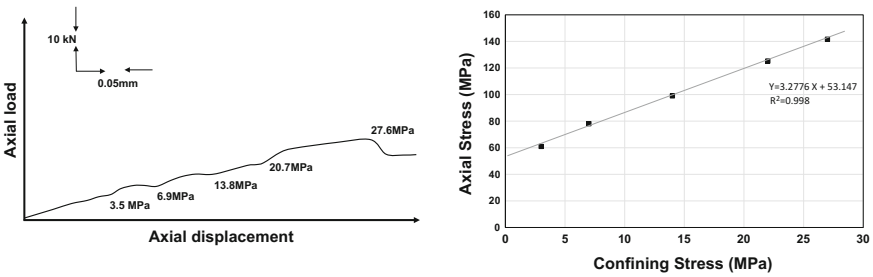

Fig. 6.5 Example multi failure axial stress/confining stress plot

From the multi-failure axial stress/confining stress results, a linear function is fitted to the data, which can be expressed in terms of the principle stress as follows (Fig. 6.5):

$$\sigma_a = UCS + \sigma_r k \tag{6.3.4}$$

where σ_a is the axial stress, σ_r the radial (confining) stress, *UCS* the uniaxial compressive stress and k the triaxial stress factor. Cohesion (So) is calculated from:

$$So = UCS/(2\sqrt{k}) \tag{6.3.5}$$

and the angle of internal friction (φ) is calculated from Eq. 6.3.3.

Along with conventional rock mechanical testing procedures, there are a number of further mechanical tests that enhance our understanding of the mechanical properties of storage reservoir and cap rocks:

- Acoustic emission (AE) describes the sound waves produced when a material undergoes stress as a result of an external force. Acoustic emission sensors detect stress waves motion that cause a local dynamic material displacement and convert this displacement to an electrical signal. Acoustic emissions can be used to detect plastic deformation indicator and crack propagation rate.
- Dynamic rock mechanical properties low and ultra-low (static) frequency experiments can be conducted to increase accuracy of the dynamic moduli measurements. This is because both P-wave and S-wave velocities increase as frequency increases from low frequency to ultrasonic frequencies. Ultrasonic data can overestimate velocities at lower frequencies, changing Young's modulus (less so for Poisson's Ratio).
- Compressibility is a measure of the relative volume change of a fluid or solid as a response to a stress change. The compression measurement procedure requires the servo hydraulic controlled stiff compression rig to have a double acting attenuator, with an integral displacement transducer (LVDT) incorporated in the actuator providing an electrical signal proportional to the piston rod displacement, this facilitates the determination of the sample compressibility.

6.3.3 Implications and Remaining Issues for CCS

All the experimental methods described above will provide mechanical property input data for the reservoir model, however they are snapshot measurements and it is important to remember that the CO_2 injection and storage system is a dynamic system that changes over time. As injected CO_2 changes the in-situ stress state, temperature, fluid density and formation water pH the fluid/rock/chemical interactions instigate changes in the porous network and in turn the elastic and strength properties of the rocks. It is important to understand how these mechanical properties evolve over time within the storage system.

6.3.3.1 Rock Mechanical Changes on Exposure to CO_2

Reservoir rock will not fail due to fluid flow alone, but as a result of stresses acting in the near well bore area. These stresses are caused by the pressure difference between the formation fluids and wellbore, fluid frictional forces, the reservoir stress state, thermal stresses and changing chemistry. When the magnitude of the combined forces exceeds the strength of the formation, the rock will fail. The key to wellbore stability is that the stresses acting on the rock surrounding the wellbore must not exceed the strength of the rock. There are a number of wellbore stability (sanding) predictors that require the rock mechanical input data of uniaxial compressive strength, dynamic shear modulus, poisons ratio, bulk modulus, modulus of elasticity, cohesion and angle of internal friction, Table 6.1.

Although the required rock strength and required mechanical input data can be experimentally determined before injection by the testing methods described above, they do not take account of the changing nature of the mechanical parameters as CO_2 injection progresses and the fluid/rock/chemical interactions instigate changes in the porous network and in turn the elastic and strength properties of the rocks. An empirical relationship must be developed between the reservoir and cap rock and its change in mechanical properties due to CO_2 exposure over time under in-situ conditions. There is no single downhole tool that can directly measure the rock

Table 6.1 Inputs in stability prediction models

Wellbore stability prediction model	Calculation—required mechanical inputs
Stein and Hilchie (1972)	Dynamic shear modulus
Stein et al. (1974)	Dynamic shear modulus
Tixier et al. (1975)	Poisson's ratio, shear modulus and bulk modulus
Coates and Denoo (1980)	Poisson's ratio, modulus of elasticity, shear modulus and bulk modulus
Risnes et al. (1982)	Cohesion and angle of internal friction
Morita et al. (1987)	Poisson's ratio, modulus of elasticity
Weingarten and Perkins (1992)	Cohesion and angle of internal friction
Sarda et al. (1993)	Effective stress, uniaxial compressive strength

elastic and strength properties of the in-situ reservoir rocks and fewer to capture the changing in mechanical properties with CO_2 injection.

Mechanical properties can be determined by the following downhole methods:

- Deformability tests that apply load to the rock surface exposed on the borehole wall and measure the resulting deformation. This can derive static mechanical properties, but this is limited to the modulus of elasticity and can only be conducted before cement casing.
- Acoustic travel times and bulk density from downhole logging, can be applied to empirical relationships relating compressional wave velocity, shear wave velocity and bulk density to the dynamic elastic parameters of modulus of elasticity, Poisson's ratio, bulk compressibility and shear modulus.
- Application of empirical correlations of porosity, composition and texture to calculate mechanical properties, (Edlmann et al. 1998).
- Indirect measurements contributing to the understanding of the mechanical nature of the reservoir such as borehole integrity from the calliper log, lithology determination and fracture identification from core, logging and wellbore imagery.

In addition to poor down-hole measurement of the mechanical properties there is little understanding of how the changes in fluid and matrix properties with the injection of CO_2 will impact on these measurements and these issues need addresses.

6.3.3.2 Remaining Mechanical Issues for Underground CO_2 Storage

There are limited studies into the effect of CO_2 injection on the mechanical properties of reservoir and caprock and the important highlights of these investigations are:

- Oikawa et al. (2008) conducted tri-axial experiments using Berea sandstone under simulated geological storage conditions and found the Modulus of Elasticity and Poisson's ratio to be suppressed slightly in the presence of CO_2.
- To undertake rock physics modeling of CO_2 bearing rocks the fluid substitution model is normally used to predict rock modulus change with a change in pore fluids, Hossain (2012), centered on Gassman's equation (Gassman 1951) input parameters are the effective bulk modulus of the rock matrix the shear modulus of the CO_2 bearing rock and the porosity. However these are input as static values and the impact of how the CO_2 bearing fluid may change these properties are not included but may have an important influence over time.
- The thermal, hydrodynamic and chemical process described in Chaps. 3 and 4 will contribute to altering the mechanical properties of the reservoir and cap rock during the CO_2 injection and storage process. Understanding the dynamic relationship between CO_2 exposure and mechanical properties influenced by mineralogy, grain size, porosity, cement depositional environment, etc. is a crucial area of research.

6.4 Fluid-Rock Interactions and Properties Changes

This section gives an overview of the experimental techniques used for investigating the mass transfers between the water-CO_2 mixture flowing in the pore space and the rock-forming minerals. Standard techniques using static or flooded reactors (*batch reactor*) dedicated to measure mineral solubility values and speciation will be only briefly outlined because they have been described in several publications and used for decades for applications ranging for instance from subsurface pollution, ore-deposit studies and hydrothermal processes (Sect. 6.4.2). Conversely we will focus on specific equipment dedicated to reproduce both the hydrodynamic and thermodynamic conditions expected during CO_2 storage operations (Sect. 6.4.3). More specifically, this type of a laboratory apparatus is designed to reproduce the pressure, temperature, fluid flow and chemical conditions. Accordingly, this kind of equipment, which is also used for studying other dynamic reactive geological settings, such as hydrothermal systems, are often called *flow-through rock* (*or reaction-percolation*) *experimental bench* or for specific application to CO_2 geological storage: *CO_2 sequestration evaluation flow system.* In the following we will use the acronym FTS (flow-through system) for simplification.

The experimental protocols attached to FTS aim at measuring the chemical fluxes and the changes of the rock properties, i.e. the change of the petrophysical, hydrodynamical and mechanical characteristics induced by the alteration of the solid fraction of the porous or fractured geomaterial under consideration. Some companies propose this type of equipment derived from those used in oil-industry for simulating multiphase flow or testing enhanced oil recovery techniques, the injection of scCO_2 being one of these techniques. Yet, experimental tools fully dedicated to study CO_2 underground storage are often designed and operated by academic research centers for specific objectives and therefore might display different technical characteristics. Nevertheless, the concepts are similar and we will outline the general technological characteristics and illustrate the use of these tools for studying mass transfer processes occurring into the reservoir during CO_2 injection, but also for studying scenarios of leakage into fractured caproks and well cement annulus (Sect. 6.4.4).

The rationale (Sect. 6.4.1) for developing specific equipment and performing such experiments coupling flow and reaction emerges from the complexity of the thermo-hydro-chemical mechanisms controlling the alteration of the rocks in the context of the forced injection of potentially highly reactive water-CO_2 mixture into potentially heterogeneous geomaterials. As a consequence modeling such mechanisms at reservoir scale is still challenging and requires not only a pertinent parameterization of the continuum approach-based modeling codes, but also to determine the validity of the underlying concepts and the accuracy of the numerical tools. Uncertainties concern essentially the integration of the heterogeneity into the macroscopic models (Chap. 5), the verification of the validity of the hypothesis used to derive the continuum approach formulation (Chap. 3) and the measurement of the effective parameters, such as the reactive surface area for example.

6.4.1 Rationale

The injection of CO_2 into deep reservoirs leads to large chemical disequilibrium and consequently can cause noticeable mass exchanges by mineral dissolution and precipitation that in turn may change strongly and often irreversibly the hydrodynamical and mechanical properties of the reservoirs. This is particularly important in the vicinity of the injection well where both the disequilibrium between the pore-fluid enriched in CO_2 and the rock-forming minerals and the fluid velocity (i.e. the renewing of the reactants) are large. Well cement and caprock can also encounter dissolution and precipitation in case of leakages through fractures either induced by overloading pressure during injection or reactivated by tectonic events.

In such conditions some of the usual assumptions supporting the validity of the macroscopic or continuum scale mass conservation equations may not be satisfied. For instance, the full mixing assumption, implying that the concentration is homogeneous at the scale of the support volume, used to derive the continuum scale advection-dispersion-reaction equation that model solute transport in porous media (see Chap. 3) may be invalid. For these dynamic systems displaying far-from-equilibrium conditions, not only pore scale concentration gradients may take place but mass fluxes controlling the return to equilibrium are non-linearly related to local concentration. Self-organized dissolution features, that tend to noticeably increase the hydrodynamic and mechanical properties heterogeneity, are expected. In other words, CO_2 injection in deep reservoir can trigger conditions in the reservoir, caprock and well cement for which the continuum scale (at which the pore scale structure and mass transfer mechanisms are averaged) approach may not preserve some aspects of the dynamics at the micro-scale. Yet the system will ubiquitously tends to return to equilibrium and therefore a very large range of conditions of flow, solute transport and dissolution-precipitation reactions are expected along the flow path from the injection well to the far field. Figure 6.6 illustrates typical trends of the Peclet (Pe_λ) and Damköhler (Da_λ) numbers as the function of the distance to the injection point. These two parameters are classically used to evaluate the hydrodynamic and hydrochemical conditions respectively. The Peclet (Pe_λ) number for a support volume of characteristic distance λ is conventionally written

$$Pe_\lambda = V\lambda/D \tag{6.4.1}$$

where V [m s^{-1}] is the average velocity and D [m^2 s^{-1}] denotes the dispersion or the diffusion coefficient depending on the studied scale. The Damköhler number (Da_λ) denotes the ratio of the characteristic time of the reactant renewing process at the reactive surface of the mineral to the characteristic time of reaction. Different formulations can be found in the literature depending on whether the renewing of the reactant is controlled by diffusion or advection, i.e. depending on the value of Pe. Here we propose a generalized definition of the Damköhler number:

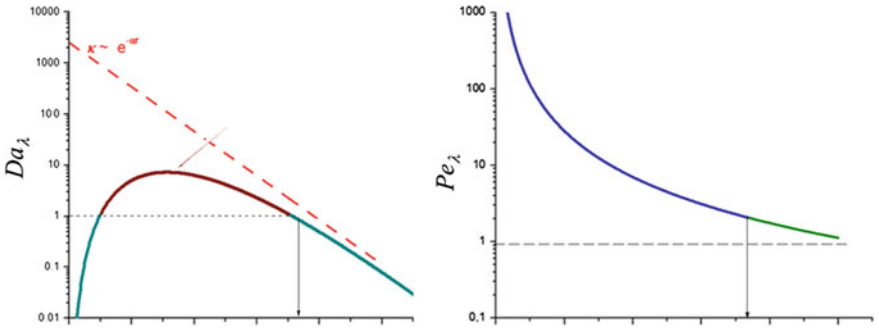

Fig. 6.6 Peclet (Pe_λ) and Damköhler (Da_λ) numbers as the function of the distance (r) from the injection point. Because the fluid velocity is proportional to the inverse of the distance in radially divergent flow, $Pe_\lambda \propto 1/r$. Conversely, the Da values may display more complex ternds as the function of r. Here we assume for matter of illustration that κ decreases exponentially with the distance to the injection ($k \propto e^{-\alpha r}$) but in reality the expression of $\kappa(r)$ is the result of complex coupling between the hydrodynamic transport and the multi-component reactions. Nevertheless it is expected that $\kappa(r)$ is a monotonic decreasing function of r because the system tends to equilibrium (i.e. $\kappa = 0$) far from the injection

$$Da_\lambda = \kappa\lambda/V\left(1 + Pe^{-1}\right) \tag{6.4.2}$$

where κ is the effective reaction kinetic velocity [s^{-1}]. The expression of κ is generally derived from the Transition State Theory (see Sect. 6.4.2). Figure 6.6 shows that a large range of conditions combining different values of Pe_λ and Da_λ can be expected. Close to the injection, large flow rate acts to maintain the system far from equilibrium whereas thermodynamical equilibrium is reached at a certain distance from the injection. Between these two extremes situations mass transfers locally dominated by diffusion, dispersion, advection or kinetically controlled reactions may occur. Similarly, a large range of hydrodynamic and hydro chemical conditions can be expected in fractures crossing caprock layers or well cement annulus depending on the differential pressure acting at the fracture boundaries and on the aperture.

A large number of experimental and theoretical studies, not specifically applied to CO_2 storage, has been devoted to study the influence of dissolution processes on the physical and chemical properties of porous media (e.g. Noiriel et al. 2004; Hoefner and Fogler 1988; Rege and Fogler 1987; Schechter and Gidley 1969). For instance, leading mechanisms such as pore coalescence (Schechter and Gidley 1969) and the formation of highly conductive flow channels (Carroll et al. 2013; Golfier et al. 2002; Renard et al. 1998; Daccord et al. 1993) involve particularly complex feedback effects. Yet, as a matter of fact the large number of studies related to CO_2 storage has boosted the construction of experimental apparatus specifically designed for using brine and CO_2 mixture for a large range of pressure and temperature. An overview of the equipment and studies is proposed in Sects. 6.4.2 and 6.4.3.

6.4.2 Batch Experiments

This section outlines the batch experiments undertaken to investigate the rock—CO_2 fluid interactions, the theory of which has been presented in Chap. 3. A brief summary of batch reactor and reaction kinetic theory is presented followed by descriptions of experimental batch equipment and analysis techniques used for instance within the MUSTANG project to characterize the fluid–rock interactions processes.

6.4.2.1 Batch Reactors

A batch reactor is a heated vessel where reactants are placed and reactions are allowed to proceed for a given time. It is designed for recurrent sampling of the fluid for analysis. The concentration and temperature are assumed to be uniform (sometimes the vessel is equipped with a stirrer) and all elements spend the same time in the reactor to ensure the same residence time. From a thermodynamic standpoint, a batch reactor represents a closed system. The system will tend to thermodynamic equilibrium with time. Batch reactors are typically used to study reaction kinetics under controlled conditions. It can be used to find reaction rate constants, activation energy and to determine the order of the reactions.

6.4.2.2 Rate Law Basics

For nearly all forward reactions, the rate is proportional to the product of the concentrations of the reactants, each raised to some power. For the general reaction:

$$aA + bB \leftrightarrow cC + dD \tag{6.4.3}$$

The instantaneous sample-averaged mass-transfer rate R [mol m^{-3} s^{-1}] can be modeled using the transition state theory (Lasaga 1998):

$$R = r(1 - I)^{-m} \tag{6.4.4}$$

where r is the effective rate constant and I the saturation index, $I = IAP/K_{eq}$, with IAP the Ion Activity Product and K_{eq} the equilibrium constant. The higher the r value is, the faster the reaction proceeds. The effective rate is usually defined as the product of the intrinsic kinetic constant r' [mol m^{-2} s^{-1}] that denotes the net flux of the reactant, by the reactive surface area σ [m^2 m^{-3}]. For CO_2 storage conditions, values of r' determined from batch experiments for different dissolution and precipitation reactions can be found in Pokrovsky et al. (2009) and references herein.

Two types of analysis are usually involved for determining the rate law for a given reaction:

- Integral method—A reaction rate is assumed and the initial ratios of concentration are known. If the final molar concentrations are plotted against time and the data fits a straight line, then the assumption of second order kinetics is true and the rate constant may be calculated from the slope of the line.
- Differential method—A reaction rate order is assumed, concentration versus time data from the batch experiments are plotted and tangents drawn at various points. The slopes of these tangents are the rate of reaction at these concentrations.

Chemical reactions are often classified according to their kinetics order:

- Zero order—the reaction rate is independent of the reactant concentration values. A change in temperature is the only factor that can change the rate of a zero order reaction.
- First order in the reactant—The reaction rate is proportional to the concentration of one reactant, e.g. radioactive decay.
- Second order in the reactant—the reaction rate is proportional to the product of the concentration of two reactants, or to the square of the concentration of a single reactant. Many dissolution and precipitation reactions are second order reactions.

6.4.2.3 Equipment Overview

Different batch reactor systems have been designed to investigate a wide variety of rock-CO_2-brine interactions under a large range of in-situ pressure and temperature conditions up to 20 MPa and 200 °C respectively. The experiments involve brine and/or CO_2 and powdered (to provide the maximum surface area for reaction) single minerals or multi-mineral rock, rock chips or rock samples. Similar experiments can be performed to study the reactions with well cement materials.

The reactor itself can be as simple as a tube (stainless steel, titanium or hastelloy) equipped at one end by a CO_2 inlet with close off valve and at the other end a 60 micron filter and a pressure release valve set at a given pressure. The tube is wrapped by a heating tape with a thermostat. More sophisticated types of reactor are often used to improve the sampling or the control of the fluid composition. For instance a reaction vessel within a pressure vessel such as presented in Fig. 6.7 can be used perform single phase experiment (only CO_2-rich brine and rock) and allow the sampling of the brine in the course of the experiment without modifying the pressure.

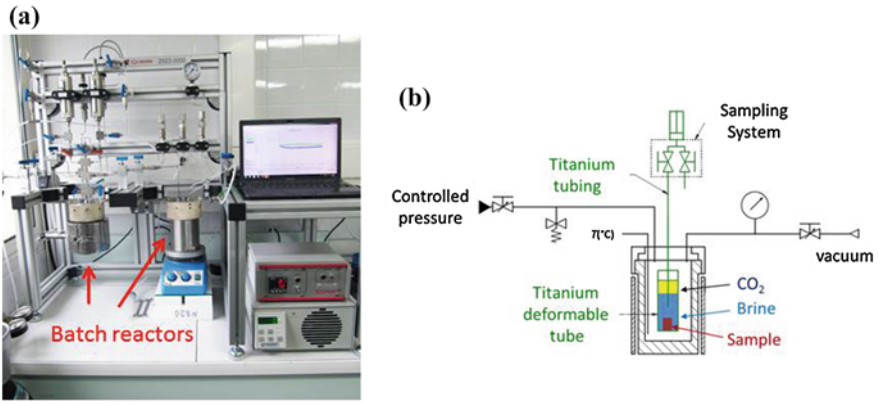

Fig. 6.7 High temperature, high pressure brine and CO_2 batch equipment. *Left* ICARE Lab stirred and non-stirred reactors. *Right* Reactor equipped with deformable titanium jacket

6.4.2.4 Analysis Techniques

There are a number of analytical techniques for measuring the fluids, gases and rock chemistry. The fluid analysis is divided into fluid element and gas composition analysis:

Element Concentrations

Major elements are routinely measured using ICP-AES (inductively Coupled Plasma Atomic Emission Spectrometry). A plasma source is used to dissociate the sample into its constituent atoms or ions exciting them to a higher energy level. They return to their ground state by emitting photons of a characteristic wavelength depending on the element present. The light is recorded by an optical spectrometer which when calibrated against standards provides a quantitative analysis of the sample.

Minor and trace elements are measured with ICP-MS (Inductively Coupled Plasma Mass Spectrometry). A plasma source is used in the same way as the ICP-AES, however the emitted ions are extracted through a series of cones into a mass spectrometer, usually a quadrupole. The ions are separated on the basis of their mass-to-charge ratio and a detector receives an ion signal proportional to the concentration.

Titration method is also often used, for example to measure the alkalinity and the chlorine content. Chemical equilibrium is a function of the concentrations of the fluids in equilibrium. The equilibrium constant value can be determined if any one of these concentrations can be measured. The concentration of the fluid in question is measured for a series of solutions with known analytical concentrations of the reactants. Titration is performed with one or more reactants in the titration vessel and one or more reactants in the burette. Knowing the analytical concentrations of reactants initially in the reaction vessel and in the burette, all analytical concentrations can be derived as a function of the volume (or mass) of titrant added.

Gas Compositions

In situ Raman analysis: A spectroscopic technique based on inelastic scattering of monochromatic light, usually from a laser source. Inelastic scattering means the frequency of photons changes on interaction with a sample and the frequency of the re-emitted photons are shifted in comparison with the original monochromatic frequency called the Raman Effect. Which when calibrated against standards provides a quantitative analysis of the sample.

Infra-red analysis: Infrared spectroscopy exploits the fact that molecules absorb specific frequencies that are characteristic of their structure. These absorptions are resonant frequencies, i.e. the frequency of the absorbed radiation matches the transition energy of the bond or group that vibrates. The exact frequency at which a given vibration occurs is determined by the strengths of the bonds involved and the mass of the component atoms

Gas chromatography: Gas chromatography is a method of separating the components of a solution and measuring their relative quantities. A sample is rapidly heated and vaporized to separate the components by distributing the sample between two phases: a stationary phase and a mobile phase. The mobile phase is a chemically inert gas that serves to carry the molecules of the sample through a heated column. Sample components are separated based on their boiling points and relative affinity for the stationary phase, which is most often a viscous liquid (wax) within the column. The higher a component's affinity for the stationary phase, the slower it comes off the column. The components are then detected and represented as peaks on a chromatogram.

6.4.2.5 Rock Mineralogy Analysis

The rock mineral analysis can be undertaken on powdered samples or using thin sections of solid samples. Whole rock analysis is not actually a complete analysis of the rock, but describes a specific method of ore preparation followed by analysis for eleven common rock-forming elements. The procedure involves a lithium borate fusion process on a small portion of pulverized solid material. The values for the rock-forming elements are then expressed as their more common oxide compound.

Powder is used also for X ray diffraction (XRD) for identifying mineral types. XRD is based on Bragg's Law, where the atomic faces of crystals cause an incident beam of X-ray beams to interfere with one another as the leave that crystal at certain angles of incidence (θ):

$$n\lambda = 2d \sin\theta \tag{6.4.5}$$

where d is the distance between atomic layers and (λ) is the wavelength of the incident X-ray beam and n in an integer. XRD measurements are based on observing the scattered intensity of an X-ray beam hitting a sample as a function of

incident and scattered angle, polarization, and wavelength or energy. X-ray Powder diffraction facilitates qualitative identification of minerals in all rock types, measure the average spacing between layers of atoms, determine the orientation of a single crystal and determine the crystal structure.

X-ray fluorescence (element quantification): X-ray fluorescence (XRF) is when a sample is exposed to X-rays of high energy. As the X-ray (or photon) strikes an atom (or a molecule) in the sample, energy is absorbed by the atom. If the energy is high enough, a core electron is ejected out of its atomic orbital. An electron from an outer shell then drops into the unoccupied orbital, to fill the hole left behind. This transition gives off an X-ray of fixed, characteristic energy that can be detected by a fluorescence detector. The energy needed to eject a core electron is characteristic of each element, and so is the energy emitted by the transition.

Thin sections are used for microscopy observation, specifically using electronic microscopes. Scanning Electron Microscopy (chemical observation and structural properties): A tungsten filament source produces a stable and high current electron beam. When the electron beam interacts with the sample, the electrons lose energy by repeated random scattering and absorption within a teardrop-shaped volume of the specimen known as the interaction volume. The size of the interaction volume depends on the electron's landing energy, the atomic number of the specimen and the specimen's density. EDS (energy dispersive) X-ray analysis: The PGT Spirit EDS X-ray analysis system allows qualitative and quantitative mineral analysis as well as X-ray imaging of samples. The number and energy of the X-rays emitted from a specimen are measured by an energy-dispersive spectrometer. As the energy of the X-rays are characteristics of the difference in energy between the two shells, and of the atomic structure of the element from which they were emitted, this allows the elemental composition of the specimen to be measured.

6.4.3 Flow-Through Experiments

A flow-through experiment consists in injecting a fluid at a controlled flow rate through a sample of permeable rock, usually of cylindrical shape, called a core. The fluid can be a single phase fluid, such as liquid water containing dissolved ions and gases or a mixture of phases. The permeable sample can be a core of porous reservoir rock or a core containing natural fractures or fractures made artificially to mimic natural hydraulic discontinuities. The main goal of these dynamic experiments involving reactive fluids is to determine the time-elapsed change of the sample properties at macroscopic scale (i.e. core scale) such as permeability and porosity and to measure effective reaction rates in dynamic conditions. Moreover, these experiments can be associated with X-ray microtomography in order to observe directly the spatial distribution of the mass transfers with a resolution of some microns. The cores are usually imaged before and after the experiment. X-ray non-absorbent confinement cells can also be used to perform recurrent imaging and tackle simultaneously the changes of the pore structure and the absolute

displacement of the different phases in the porosity. Nevertheless, the use of this technique is presently limited by several factors such as the duration of the experiment, the possibility of working at elevated pressure and temperature and the duration of the scan (largely dependent on the X-ray source flux and the sample size) during which it must be assumed that mass transfers are negligible. In any case, the sample size must be decided in order to fit the field of view of the camera; higher is the targeted resolution, smaller is the core diameter. In most of the cases core diameter (D) ranges from few millimeters to few centimeters and the geometrical resolution ranges from 0.5 to 20 microns depending on the applied imaging techniques.

The duration of the experiments typically ranges from some hours to weeks. For example, the alteration of a carbonate rich reservoir core flowed by a CO_2-saturated brine at 50–90 °C can be studied in few days, while the same conditions applied to the study of sandstones or fractured cements and claystones may require weeks.

6.4.3.1 FTS Equipment

As a general rule, the system includes motorized pumps equipped with displacement encoders which allow an accurate control of the inflow rate, a confinement cell were the sample is installed, heated and pressurized and a back pressure system allowing to control the outlet pressure while allowing the fluid to be withdrawn from the circuit and sampled for chemical analysis. A schematic representation of a flow-through apparatus is given in Fig. 6.8.

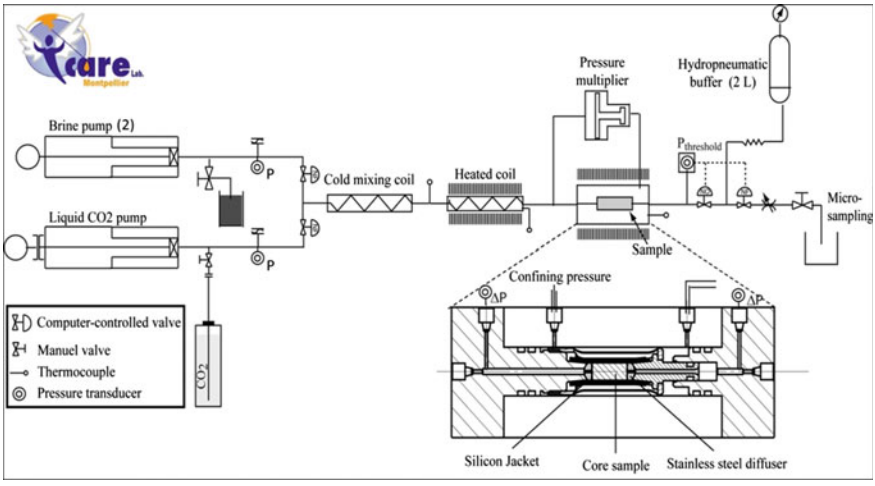

Fig. 6.8 Schematic representation of the ICARE Lab CO_2 sequestration evaluation flow system (model ICARE 1, design R. Leprovost, U. Montpellier)

A standard circuit requires up to 20 valves, most of them being usually electro-pneumatic valves (EPV); their opening and closing being mastered by the computer program which also control the pump flow rate.

The back pressure system is probably the most critical part of the FTS and different techniques can be used as it will be explained below. The second critical issue for reproducing the range of reservoir conditions is the flow rate. Modern computer controlled piston pump can deliver flow for a large range of values, but the main issue is often the capability of controlling the very low flow rates required to mimic in situ condition in small sized samples. Delivering low flow rate implicates the use of pumps having small pistons and high-technology motors and position encoders. Going down to flow rate of less than about 10^{-11} m^3 s^{-1} ($\sim 10^{-3}$ mL min^{-1}) requires specialized equipment using high-end pumps and a precise control of the temperature.

Others issues to be considered when designing such experimental bench for temperature up to 150 °C include the corrosive nature of the fluid (usually low pH brines) and the need of accurate temperature control and adapted circuit geometry when mixtures of $scCO_2$-water (or brine) are involved. Usually corrosion resistant alloys such as Hastelloy- C276 are used at least for the most exposed parts such as the pumps, the valves, and the pressure sensor membranes. The use of accurate and well calibrated pressure sensors is also required in order to obtain accurate values of the permeability over 2 or possibly 3 orders of magnitude. For some applications it is beneficial to set the pressure gradient instead of the flow rate. In this case the flow rate is measured from the displacement of the pump piston or counting the motor axe rotation using optical or electronic encoders.

Inlet Pumps: A combination of two piston pumps is required to obtain a constant flow rate for injection volumes larger that the volume of one pump. In this configuration, one of them pumps the liquid through the sample, while the other one refills from and external fluid tank. This procedure is controlled by a microprocessor installed in the pump electronic control card or directly by a computer. The objective of these experiments being to inject brines and CO_2 through the sample for a large and controlled range of partial pressure values, the question of mixing the CO_2 with the brine is a central issue. Two cases can be distinguished.

If the objective is to pump brine in which the partial pressure is lower than the total pressure, then the pumped fluid is a single phase. In this case the issue is to dissolve CO_2 into the brine in order to obtain a given constant CO_2 partial pressure whatever the total pressure is. Two main techniques can be applied. First the CO_2-brine mixture can be prepared in a tank by pressurizing the volume of brine required for the entire experiment with CO_2 at a pressure corresponding to the targeted CO_2 partial pressure. For values larger than the pressure of commercial CO_2 bottles (about 6 Mpa), the use of a pressure booster withdrawing and compressing liquid CO_2 from a bottle equipped with a plunger is necessary. This mixture will be used to refill the piston pumps. An alternative solution consists in adding to the FTS a piston pump refilled with liquid CO_2. The mixture will be obtained by running the brine and CO_2 pumps at the flow rates corresponding to the fraction of CO_2 needed

to obtain the desired CO_2 partial pressure. As the volume of CO_2 to pump is only few percent of the volume of brine, the pump dedicated to the liquid CO_2 must have a minimal flow rate about two orders of magnitude smaller than the minimum flow rate needed for the experiment. This is the limiting factor of this technique (the minimum flow rate is here conditioned by the CO_2 pump characteristics) which conversely allows changing easily the CO_2 partial pressure in the course of the experiment.

For experiments requiring the injection of $scCO_2$-brine mixture, i.e. the injection of a biphasic fluid, an additional supercritical CO_2 pump is required. Such pump consists in a cooled pressure booster that pumps liquid CO_2 from a plunger-equipped bottle and a heating system allowing the pressurized liquid CO_2 to reach the supercritical phase. Note that the differential density between liquid and supercritical CO_2 must be taken into account for calculating the effective flow rate. The use of $scCO_2$ in FTS will be discussed in more detail below.

Back Pressure: Back pressure is necessary to reproduce the conditions at depth. It is also required for avoiding degassing of the CO_2 in the circuit; the total pressure must be higher or equal to the partial pressure of CO_2 to perform single phase experiments. Mainly three techniques can be used to control the total pressure of the outlet circuit. All of them produce pressure fluctuations but with distinctly different amplitudes and frequencies. As the objective is to maintain a pressure as constant as possible, all the different systems described below must be associate with a pressure damper that usually consists in a cylinder with a free mobile piston separating the flowing fluid from a volume of pressured gas. If the pressure fluctuations are small, then the free-piston cylinder can be replaced by a membrane.

The simpler one consists in using constant pressure valves. However this type of low-cost tools may be not sufficient for maintaining a sufficiently constant pressure at low and high flow rates. These valves are also temperature sensitive. As a result, large amplitude, low frequency pressure fluctuations are expected. Moreover freezing of the valve can occur when large amount of supercritical or liquid CO_2 have to be released by the valve. Micro-particles, for instance produced by the rock dissolution, may prevent the full closing of the valve and therefore may jeopardize irreversibly the experiment.

The second system that was experienced in the frame of the MUSTANG project is the use of a combination of two EPV in series, separated by a tube of limited volume, that alternatively open and close in order to deliver a flow rate that adapts to the pressure at the outlet of the sample while keeping it in a constant range of few tenths of MPa. Using a pressure damper containing 1 L of pressured gas is usually sufficient to obtain fluctuations of less than 0.1 MPa. This system is efficient and relatively cheap, but the valves are aging very fast because of their frequent activation (usually several hundred of operation for a standard experiment).

The third system consists in using back pressure piston pumps; ideally two piston pumps acting similarly to the dual injection pumps described above. These pumps will be programmed to maintain the desired pressure by continuously adapting the pistons displacement. Yet, the use of a single piston pump can be

preferred for decreasing costs. In this case, a pressure damper containing about 1L of pressurized gas will allow pressure fluctuation to be less than 0.1 Mpa.

Sampling: sampling for cations analysis can be performed after degassing at the outlet of the circuit. However it is often necessary to sample the pressurized brine mixture or brine-CO_2 mixture, for evaluating the remaining CO_2 partial pressure, for instance. High pressure syringe with a screw-moving piston can be used. A simple technique for evaluating the CO_2 partial pressure is to equip the syringe with a micrometric screw gauge and a pressure sensor (or manometer) and measure the volume of gas released from the adiabatic decompression of the sample. The partial pressure (P_{CO_2}) is:

$$P_{CO_2}(P,T,s) = P_e \times P_d \times V_{dg}/R \times T \times V_L \times mCO_2(P,T,s) \tag{6.4.6}$$

where P_e and P_d denotes the pressure of the experiment and the pressure after decompression, V_{dg} and V denotes the volume of gas after decompression and the volume of the fluid sampled, R is the gas constant, T is the temperature and $m\mathrm{CO}_2$ is solubility of CO_2 (Duan et al. 2006; Sun and Dubessy 2010).

Core Sample Holder: There are several designs of sample holder, named also confinement cell. Several providers propose standard designs such as Hassler type or Hoek type core holders adapted to different core sample sizes. Research laboratories are also developing core holders/confinement cells, usually to fit non-standard sample size. Whereas these different types of cells differ from each other in terms of technical details impacting mainly the protocol for the sample installation, the principle is similar for all the sample holder types. The cylinder of rock is installed into a flexible tube (or jacket) that can be made of different substance such as silicon, Teflon or vulcanized materials and then positioned in between two flow diffusers such as displayed in Fig. 6.8. This configuration allows applying an external pressure on the jacket ensuring that the fluid will not flow around de sample but is distributed equally over the sample diameter. This applied pressure is also used to reproduce de confinement pressure at depth (radial confinement pressure). Axial pressure mimicking the effect of the overburden along the sample axis can also be setup (Fig. 6.8). The axial and radial pressure can be operated by external piston pumps, gas tanks or made proportional to the inlet flow pressure using a pressure multiplier such as shown in Fig. 6.8. This later solution has two advantages; first it is unexpansive compared to the purchase of piston pumps and second it ensures that the confinement pressure increase (or alternatively decrease) proportionally to the fluid pressure during the operation of pressure loading (or unloading) at the beginning and end of the experiment, avoiding deviatoric stresses that may damage the sample irreversibly. In general it is sufficient to apply axial and radial pressures of about 110–115 % of the pore pressure for ensuring both a total sealing of the sample-jacket interface and reproduce natural pressure configurations.

Control of the Composition of the Inlet Fluid: Controlling the composition of the inlet fluid (brine) is important to reproduce the natural conditions. The ionic content can be set easily, but controlling the partial pressure of the gas requires some

attention. This aspect, often disregarded in flow-through experiments, is important for example to reproduce anoxic conditions such as almost always the case in reservoirs, or even impose partial pressure of secondary gases such as methane of hydrogen to reproduce reducing conditions. A specific device has been developed in the frame of the MUSTANG project in order to make a controlled preconditioning of the brine, before being mixed with the CO_2. This device, called *ICARE Lab Fluid Preconditioner*, permits removing or adding dissolved gases or tracers in the fluid and keeping this volume of fluid (up to 5 L) under a pressure of 0.8 MPa during the duration of the experiment. The piston pumps will be refilled from this pressurized tank.

Use of $scCO_2$: The conceptual design made by the different functional parts of a flow-through bench presented above (synthetized by the schema given in Fig. 6.8) is designed primarily to single phase flow experiments for which the partial pressure of CO_2 can be set from zero up to the minimum value of the pressure in the circuit, i.e. the pressure set by the back pressure system. However, one may want to simulate the flow of pure $scCO_2$ or mixture of $scCO_2$ and CO_2-saturated brine. In this case one must install a $scCO_2$ pump that is made of three components. The central part of the pump is a pressure booster that withdraws liquid CO_2 from a CO_2 bottle equipped with a plunger. To ensure a perfect functioning, the booster pump is cooled down to few Celsius (generally 4 or 5 °C) by a cooling system. On the high pressure side of the pressure booster the CO_2 is heated to the desired temperature (above 32 °C) to produce $scCO_2$. In order to avoid any $scCO_2$ trapping in the circuit and ensure a perfect mixing the $scCO_2$ must be injected as close as possible to the sample through a diffuser.

6.4.3.2 Measurements and Data Analysis

The two main measurements allowed by flow-through experiment are the monitoring of the pressure drop in the sample and the recurrent sampling and composition analysis of the outlet fluid. The fluid analyses are performed using the different methods presented in Sect. 6.4.2.4. The pressure drop is measured by a differential pressure sensor recording the pressure difference $\Delta P(t)$ between the inlet and the outlet of the sample. Permeability $k(t)$ is obtained from the differential pressure using the Darcy law (Eq. 6.2.3) for porous media.

In case of fractured low permeability rocks (usually $<10^{-19}$ m^2 for cements and claystones), the permeability and fracture aperture $a_h(t)$ are estimated using the cubic law approximation:

$$a_h(t) = \sqrt[3]{\frac{12\mu Q L}{w\Delta P(t)}} \tag{6.4.7}$$

and

$$k(t) = \frac{a_h^2(t)}{12} \tag{6.4.8}$$

where w is the width of the fracture.

The time-resolved porosity of the sample cannot be measured directly, but in certain cases the change of porosity ($\partial\phi/\partial t$) can be evaluated from the fluid composition. The simple case is when the only chemical process is the dissolution of a single mineral. Let assume that the rock sample is made of Magnesium-rich calcite $Ca_\alpha Mg_\beta CO_3$, where and α and β denotes the fraction of Ca and Mg respectively in the calcite. The volume of dissolved calcite $V(t)$ is:

$$V(t) = \upsilon Q \int_{t'=0}^{t'=t} \alpha \Delta C_{\mathrm{Ca}}(t') + \beta \Delta C_{\mathrm{Mg}}(t') dt' \tag{6.4.9}$$

where υ is the calcite molar volume and ΔC_{Ca} and ΔC_{Mg} denotes the difference of calcium and magnesium concentration respectively between the outlet and the inlet fluids. The sample-scale porosity change of porosity is given by:

$$\frac{\partial \varphi(t)}{\partial t} = \frac{1}{V_s} \frac{\partial V(t)}{\partial t} \tag{6.4.10}$$

where V_s is the total sample volume (i.e. $V_s = \pi L D^2/4$). To evaluate the time-resolve porosity $\phi(t)$ one must integrate Eq. (6.4.10) which requires the knowledge of the value the porosity at a given time t, usually at $t = 0$. This can be achieved by non-invasive laboratory measurement using a gas porosimeter for example, or calculated from the analyses of XMT images.

When the dissolution process involves several minerals sharing the same cations or when both dissolution and precipitation occurs simultaneously, the mass balance (Eq. 6.4.9) is much difficult to calculate. However this can be completed if both the composition of the involved minerals and the stoichiometry of the reactions are known. Accurate chemical analysis of the rock sample combining different techniques such as chemical imaging using electronic microscopy, X-ray diffraction and bulk analysis may provide the necessary data. Then, if the value $V_i(t)$ for all the dissolved and precipitated minerals i can be calculated, then the change of porosity ($\partial\phi/\partial t$) is obtained by Eq. (6.4.10) where the second member $\partial V(t)/\partial t$ is replaced by the sum $\sum_i \partial V/\partial t$.

6.4.4 *Examples of Experimental Studies of Fluid-Rock Interactions*

6.4.4.1 Experimental Investigation into the Sealing Capacity of Naturally Fractured Shale Caprocks Under scCO$_2$ Flow

A high pressure and temperature CO_2 flow rig was designed and built to investigate the sealing properties of naturally fractured caprocks under in-situ conditions and supercritical CO_2 and gaseous CO_2 flow (Edlmann et al. 2013; McCraw et al. 2016). One unfractured (sample B-c) and two naturally fractured caprock 38 mm diameter core samples (Samples B-a and B-b) were obtained from the North Sea East Brae field at a depth of circa 4 km, Fig. 6.9.

In addition to the flow results, petrophysical and mineralogical data was collected from the caprock matrix and fracture surface before and after exposure to CO_2. Porosity is around 17 %, the mean pore radius around 900 nM and X-Ray Diffraction (XRD) investigations of both the caprock matrix and fracture fill material show that quartz (43 %) and illite (≈25 %) are the primary minerals that make up the Kimmeridge clay caprock, with minor chlorite (8 %) and kaolinite (8 %).

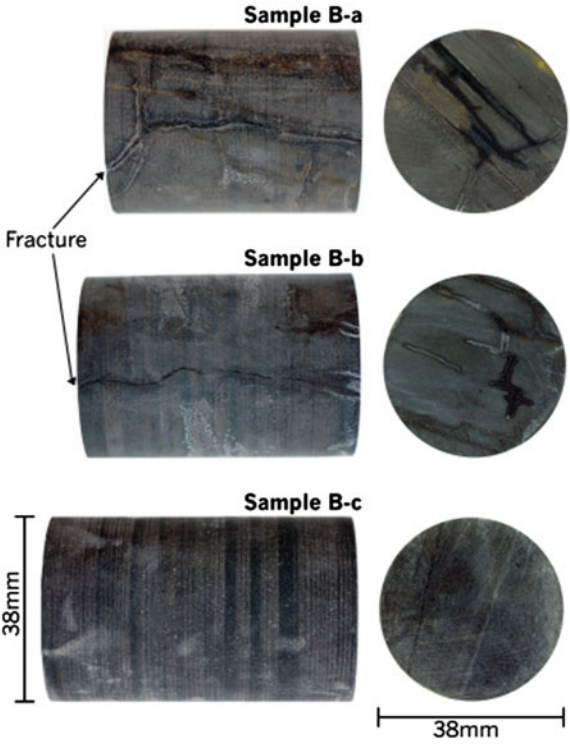

Fig. 6.9 Images of the three core samples of caprock from East Brae

The flow experiments were run in 4 phases:

- Phase 1—Increasing to in-situ $scCO_2$ conditions
- Phase 2—Maintaining in-situ $scCO_2$ conditions
- Phase 3—Maintaining in-situ gaseous CO_2 conditions
- Phase 4—Re-run of the increasing upstream CO_2 fluid pressure and lock in under supercritical and gaseous conditions to investigate wettability changes after CO_2 exposure along the fracture face

The results of Phase 1, 2 and 3 for samples B-a and B-b are presented as confining pressure (in MPa, MegaPascal), upstream pressure (MPa) and downstream pressure (MPa) on the primary axis and temperature (°C) on the secondary axis all against time (Figs. 6.10 and 6.11). There was no detectable flow of CO_2 (downstream pressure) measured across both fractured samples, even with a pressure differential across the fractured of 43 and 51 MPa, for samples B-a and B-b respectively, which equates to a pressure gradient of 866 and 942 MPa/m. As soon as the fluid pressure, confining pressure and temperature were dropped to gaseous CO_2 conditions of 20 MPa confining pressure, 5 MPa upstream pressure (the same

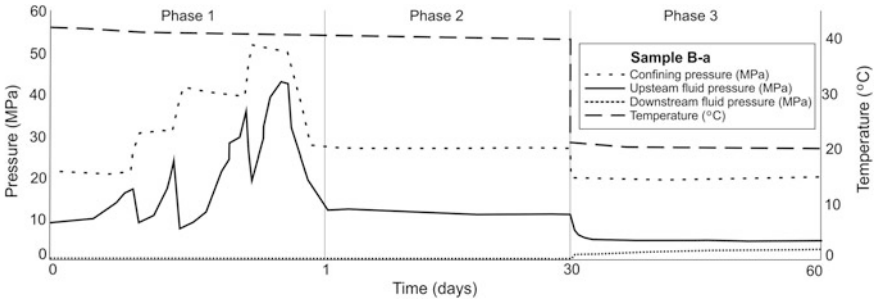

Fig. 6.10 Results of the fractured caprock sample B-a, plotted as confining pressure (MPa), upstream pressure (MPa), downstream pressure (MPa) and temperature (°C),with time

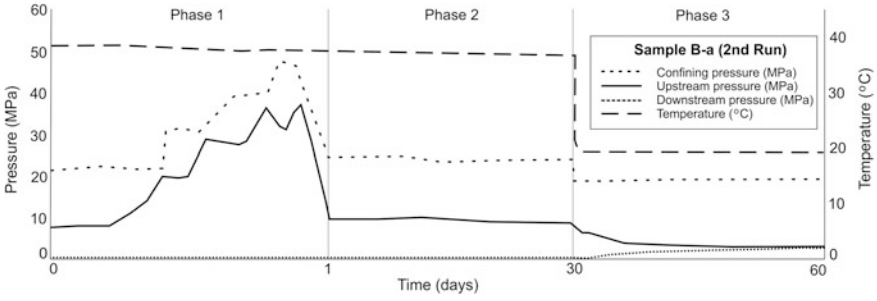

Fig. 6.11 Results of the fractured caprock sample B-b, plotted as confining pressure (MPa), upstream pressure (MPa), downstream pressure (MPa) and temperature (°C), with time

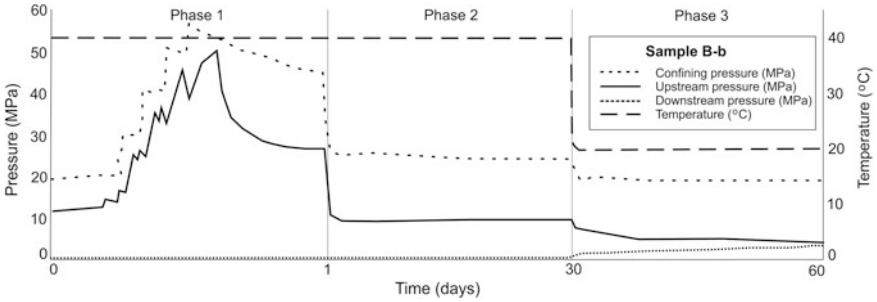

Fig. 6.12 Results of the second flow run on fractured caprock sample B-a, plotted as confining pressure (MPa), upstream pressure (MPa), downstream pressure (MPa) and temperature (°C),with time, to investigate any wettability effects after CO_2 exposure along the fracture face

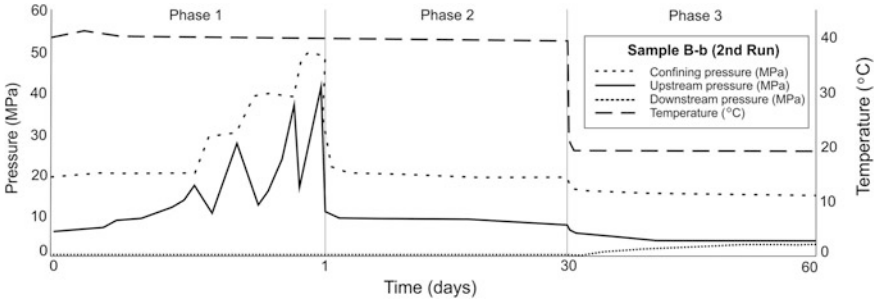

Fig. 6.13 Results of the second flow run on fractured caprock sample B-b, plotted as confining pressure (MPa), upstream pressure (MPa), downstream pressure (MPa) and temperature (°C), with time, to investigate any wettability effects after CO_2 exposure along the fracture face

15 MPa pressure difference as with the supercritical lock in) and 20 °C temperature, the downstream pressure immediately and steadily increased over the 30 days towards that of the upstream pressure. This introduces the possibility that for these particular naturally occurring fractures gaseous CO_2 does flow across the fracture, whereas there was no supercritical CO_2 flow across the fracture, even when the fracture aperture is held under the same differential pressure.

During phase 4, the re-run after gas phase CO_2 exposure to the fracture, the same pattern of pressure (flow) across the fracture was observed during the second run as was seen during the first run, Figs. 6.12 and 6.13. There was no flow measured under increasing $scCO_2$ flow even with pressure differentials of 37 and 42 MPa for samples B-a and B-b respectively. This was also under conditions of fluctuating fracture aperture linked directly to a fluctuating difference in pressure between the upstream fluid and confining pressure. There was little or no detectable flow of $scCO_2$ measured across both fractured samples under $scCO_2$ lock over 30 days. However under gaseous CO_2 lock in (with the fracture aperture held under the same pressure difference between the upstream fluid pressure and confining pressure as it

Table 6.2 Average mineral weight percentages for sample B-a matrix and fracture before and after CO_2 exposure

	wt% Al	wt% Si	wt% Ca	wt% Mg	wt% Fe
Sample B-a matrix before CO_2 exposure	7.45	37.30	0.51	0.54	0.68
Sample B-a matrix after CO_2 exposure	9.51	35.24	0.47	0.61	0.83
Sample B-a fracture before CO_2 exposure	8.21	35.86	0.55	0.51	1.17
Sample B-a fracture after CO_2 exposure	10.40	32.65	1.07	1.33	0.99

was under supercritical conditions), the same pattern of immediate and increasing downstream pressure towards that of the upstream pressure was observed.

This indicates that under these experimental conditions and timescales, the wettability (and in turn capillary entry pressures) of these natural fractures was not influenced by exposure to gaseous CO_2.

Table 6.2 presents the average mineral weight percent of the caprock matrix material and fracture material before and after the CO_2 flow experiments on sample B-a from SEM energy dispersive X-ray elemental analysis. It can be ascertained that although there was a slight reduction in Silicon (2 %) and corresponding increase in Aluminum (2 %) after exposure to CO_2 as cation exchange occurs. However it is not significant enough to cause fracture/matrix pore network opening or closing that would influence the CO_2 flow through the duration of the experiment.

This lack of any chemical reactivity is borne out by comparing the sample dimensions before and after the experiment, the confining pressure data logs also corroborate the lack of any volume changes within the samples at equilibrium during experimentation.

The conclusions we can draw from the experimental work undertaken so far on the sealing capability of naturally fractured shale caprocks to supercritical CO_2 flow are that:

- Supercritical CO_2 did not flow through these particular tight natural caprock fractures under supercritical reservoir conditions.
- When the temperature and fluid pressure were reduced to below the critical point, CO_2 in its gas phase did flow through the tight natural caprock fractures (even with a constant pressure difference between the confining pressure and the upstream fluid pressure of 15 MPa under both supercritical and gaseous conditions).
- This contradicts the expected flow profile of a supercritical fluid having enhanced flow properties.
- The contradictory experimental observations are linked to the complex interplay between the fluid conductivity response of the CO_2 phase to the fracture properties, the influence of stress on the fracture aperture, the chemical interaction between the rock minerals and the CO_2 fluid, the fluid pressure influencing the fracture permeability, the influence of CO_2 phase on the capillary entry pressure and the relationship between CO_2 phase on the wettability, interfacial tension and contact angle.

- To facilitate the observed result of gaseous CO_2 flow and inhibited supercritical CO_2 flow it is likely that the interplay between normal stress and pore pressure controlling fracture aperture and the density of CO_2 being inversely proportional to permeability were the dominant influencing factors.
- Calculations indicate that there is a large decrease in hydraulic conductivity as the aperture size reduces, indicating that it is aperture size that is the dominant controlling factor in fracture flow of CO_2. It is possible that there is a critical threshold of fracture aperture size which controls CO_2 flow along the fracture. Above the critical aperture size $scCO_2$ and gaseous CO_2 will flow, on or near the critical fracture aperture size we see gaseous flow but not $scCO_2$ flow and below the critical aperture size we would see little or no gas or $scCO_2$ flow along the fracture and flow would become matrix dominated.
- This has significant implications for the planning of CO_2 storage projects in the North Sea basin, in that the CO_2 should be stored at pressures and temperatures (depth) comfortably above the CO_2 critical point.

6.4.4.2 Experimental Investigation of the Role of Local Heterogeneities on Reactive Transport

Understanding the fundamental processes governing the fluids-rocks interactions is a crucial stake to model, for various temporal and spatial scales, the transport and the storage of CO_2. One of the major difficulties is the identification and the hierarchical organization of the involved imbricated physical and chemical mechanisms. Consequently, an essential step is to perform experiments in controlled conditions for which results can be analyzed from pore-scale to the scale of the samples.

Several percolation experiments of acid fluid (CO_2-rich brines) through different type of rock samples reproducing in situ conditions ($T < 200$ °C, $P < 20$ MPa) will be present here to enlighten the use of experimental results for characterizing the role of heterogeneities on transport and reactions processes (dissolution, precipitation, redox reactions). All the flow-through experiments presented here have been performed using the *ICARE Lab CO_2 sequestration evaluation flow system* presented in Sect. 6.4.3 and described in more details in Luquot and Gouze (2009).

The different analytical techniques mentioned in this chapter have been used in order to characterize the mineral rock composition, the pore structure and geometry, the connectivity of the core before and after each percolation experiment. Besides the classical analytical methods, SEM (Scanning Electron Microscope), Raman spectrometry, Mossbauer, Ionic probe, TEM (Transmission Electron Microscope), have been used as well as X-ray Microtomography images (XMT). As explained in Sect. 6.2.1, one can extract key parameters such as the total porosity, the effective porosity, the pore size distribution, the pore/rock interface surface, the tortuosity, the effective diffusion coefficient, the permeability and other morphological and geometrical parameters such as capillary pressure and pore surface curvature, by processing the 3D micro-tomographic images.

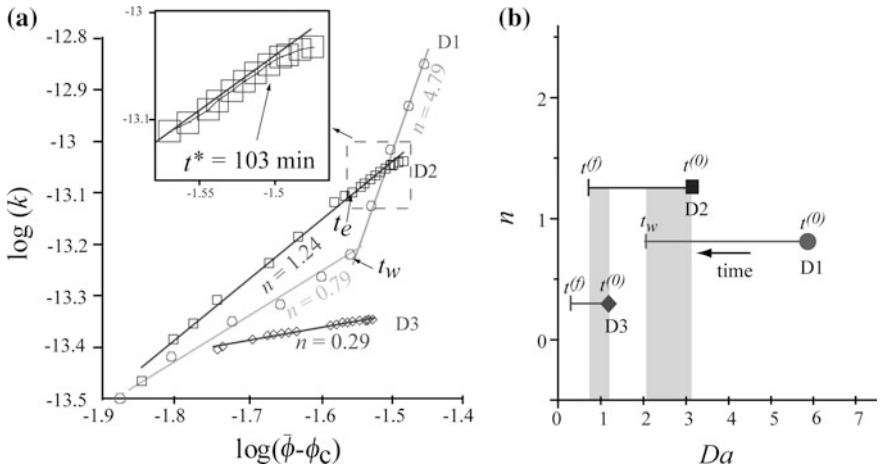

Fig. 6.14 **a** Log-permeability versus log-porosity for the dissolution experiments D1 (*circles*), D2 (*squares*) and D3 (*diamonds*). *Inset* Focus on the experiment D2 data for $t > t_e$. For $t > t^*$, data deviate progressively from the power law model. **b** Exponent n versus $Da(0)$ for experiment D1 (*circles*), D2 (*squares*) and D3 (*diamonds*). The range of $Da(t)$ for each of the experiment is reported (*horizontal lines*) as well as the overlapping between experiments D1–D2 and D2–D3 (from Luquot and Gouze 2009)

The methodology and experimental approach previously mentioned have been first applied to characterize the different dissolution patterns that occurred during CO_2-rich brine injection through limestone core samples (from Paris Basin). Various flow-through experiments have been performed using a same Peclet number but changing the Damköhler number. All the experiments have been done under CO_2 storage conditions (T = 100 °C, P = 12 MPa, $2.5 < P_{CO_2} < 10$ MPa). Various dissolution patterns have been described during the different dissolution experiments depending of the *Da* number. These dissolution features have been correlated to the flow conditions and initial chemical fluid properties: from localized wormhole formation (P_{CO_2} = 10 MPa) to homogeneous dissolution (P_{CO_2} = 2.5 MPa). The main results of these set of experiments were published in Gouze and Luquot (2011) and Luquot and Gouze (2009). In particular, the authors demonstrated that porosity, permeability and reactive surface area changes due to dissolution reaction are controlled by initial chemical conditions of the injected fluid and initial parameters (Fig. 6.14). A memory effect has been observed in the variation of all these parameters with time. A phenomenological relationship between porosity and permeability (Fig. 6.15) and reactive surface area have been proposed and later validated by others authors.

Gouze and Luquot (2011) showed that permeability changes during dissolution process are controlled by tortuosity changes in case of heterogeneous dissolution (wormhole localization formation) and to the hydraulic pore diameter in case of homogeneous dissolution (Fig. 6.15).

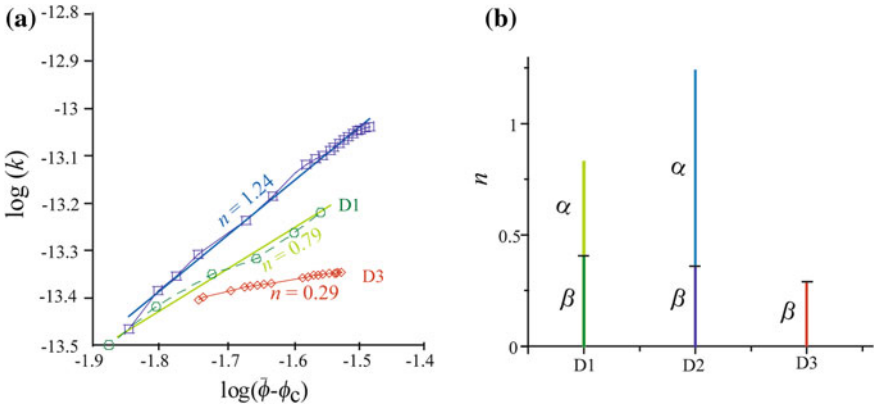

Fig. 6.15 **a** Sample-scale averaged porosity versus permeability for experiments D1, D2 and D3. **b** Values of exponent α (indicator of hydraulic radius increase) and β (indicator of tortuosity increase), with $n = \alpha + \beta$, for experiments D1, D2 and D3 (from Gouze and Luquot 2011)

Others experiments have been performed using different types of limestones confirming that the initial rock structure strongly controls the dissolution pattern and specifically the development of preferential paths and thus controls the permeability-porosity relationship (Fig. 6.14). Furthermore, experiment with lower CO_2 partial pressure using limestone samples characterized by smaller pores have be run in order to try observing homogeneous dissolution processes, but here again the formation of preferential flow path was observed (Fig. 6.16).

From these results on can propose a phenomenological relationship between tortuosity change $\Delta\tau$ and P_{CO_2} and speculated that the porosity–permeability trend is mainly controlled by the change in the effective hydraulic diameter during dissolution with low P_{CO_2} (Fig. 6.17). These results cast doubt on the use of the Peclet and Damköhler numbers to predict dissolution pattern independently on other information on the structural properties and the heterogeneity of the rock (Luquot et al. 2014).

Andreani et al. (2009) and Luquot et al. (2012) studied sandstone core samples coming from potential CO_2 storage reservoir in Australia and dunite samples coming from San Carlos, Arizona, respectively. The interesting point of these two different rocks is the complex mineralogy and the large range of chemical processes that can occur in contact with CO_2-rich brine.

The sandstone rock was coming from de Pretty Hill Formation from Otway Basin and was mainly composed of quartz and feldspar and almost 10 % of Fe-rich chamosite (chlorite) and Laumontite (Ca-rich zeolite). Two interesting processes were observed during CO_2-rich brine percolation through this sandstone: the first one was the feldspar alteration into kaolinite which induces a permeability decrease which was described for the first time. The second key result of this study was the redox reaction characterized between CO_2 and iron-rich chamosite mineral. The results show that a fraction of CO_2 was stored as reduced carbon (graphite) using

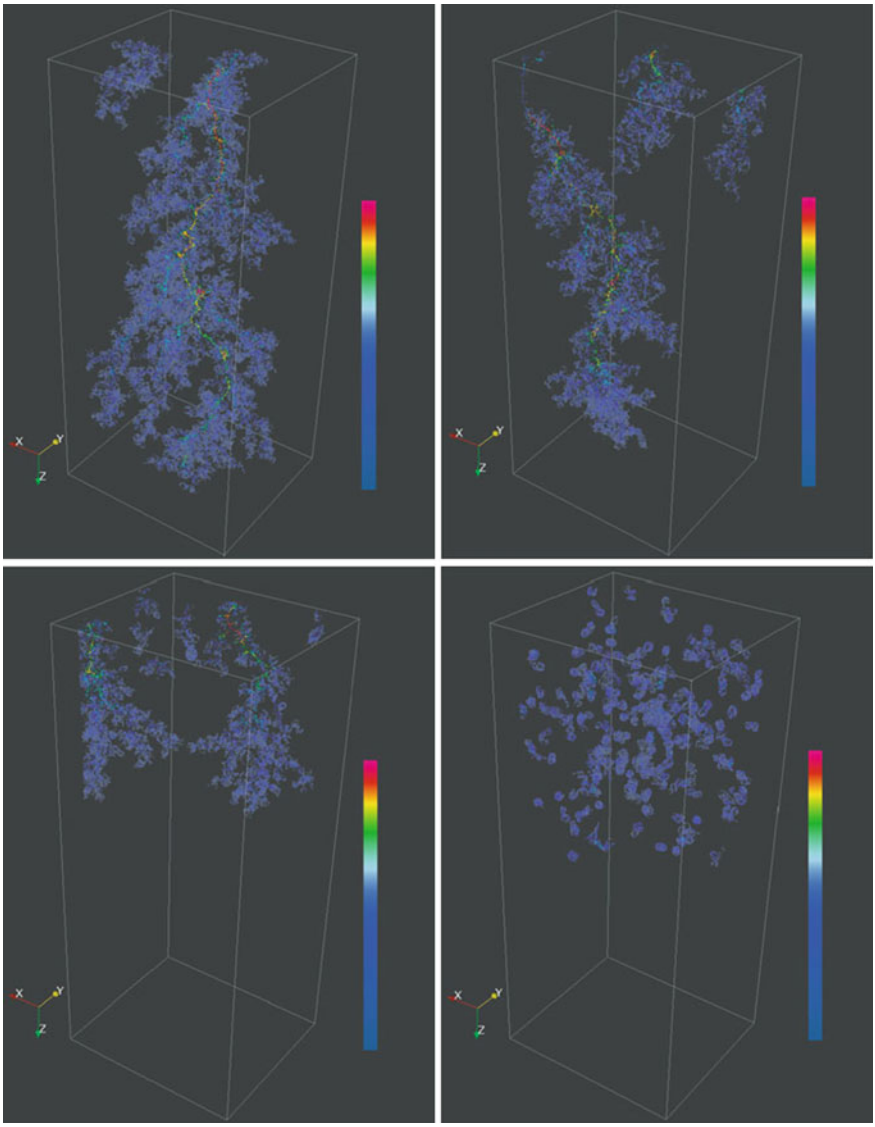

Fig. 6.16 Representation of the nodes of the main components of the skeleton, i.e., parts of the skeleton coinciding with connected components of the void space that were exposed to dissolution at macroscopic scale. The *color map* corresponds to the radius of the largest sphere centered at each node inscribed *inside* the void space (brightest points correspond to largest radii, logarithmic scale in voxel unit), from Luquot et al. (2014)

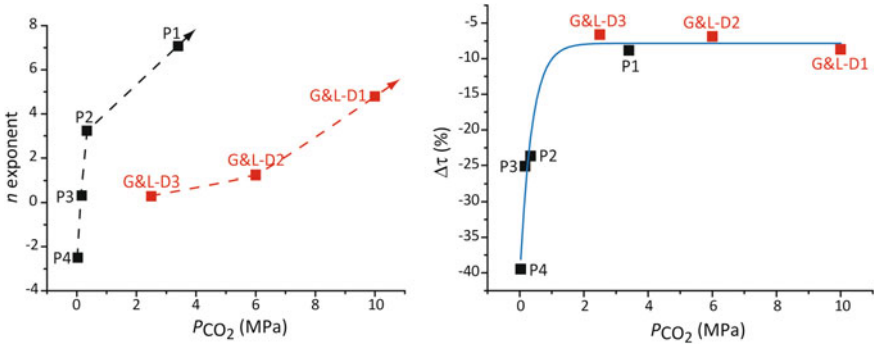

Fig. 6.17 *Left figure* Change of the exponent n of the permeability–porosity relationship versus P_{CO_2}. *Right figure* Tortuosity versus P_{CO_2}. In *black*, the results for experiments P1, P2, P3, and P4 are presented and in red the results for experiments G&L-D1, G&L-D2, and G&LD3 from Luquot and Gouze (2009) and Gouze and Luquot (2011). The *blue curve* represents the equation $\Delta\tau = y_0 + A \exp(B \times P_{CO_2})$, with $y_0 = -7.83$, $A = -33.14$ and $B = 0.37$ (from Luquot et al. 2014)

realistic conditions for CO_2 geological storage (Fig. 6.18). This study allows highlighting the role of local mineral heterogeneity on chemical reactions. As observed in Fig. 6.18, the redox reaction occurred very locally closed to chamosite dissolution features.

The study of CO_2-rich brine reaction with dunite was performed at very low flow rates and high temperature and pressure conditions. The rock sample was almost composed of olivine so in this case the initial rock was not characterized by an initial mineral heterogeneity. Nevertheless, various reactions can take place after olivine dissolution triggerd by the CO_2-enriched water: mainly serpentine precipitation (olivine hydration mechanism), carbonate precipitation (mainly Mg, Fe, Ca-carbonates), iron oxide precipitations, hydrogen production. In this study, Andreani et al. (2009) observed the localization of the different reactions depending of the local transport conditions. In zones were transport was controlled by advection, i.e. where the reactant renewal was high, olivine dissolution rate, hydration reactions and iron oxide precipitation were observed. Conversely, carbonate precipitation was observed were the reactant transport was controlled by diffusion such as in dead-end structures (Fig. 6.19). These results clearly indicate that local transport conditions controlled the product of the chemical reaction and that the assumption of *full mixing* discussed in Sect. 6.4.1 is hardly valid in such highly reactive system involving high CO_2 concentration fluids.

More recently, Luquot et al. (2016) confirmed the role of local chemical/mineralogical heterogeneity on reactive processes but also the importance of the local transport conditions. They performed CO_2, sulfate-rich brine percolation experiments at different injection flow rates through sandstone core rock samples coming from Heletz formation in Israel (MUSTANG test site). Experiments were performed under in situ Heletz storage conditions (60 °C and 15 MPa). The authors

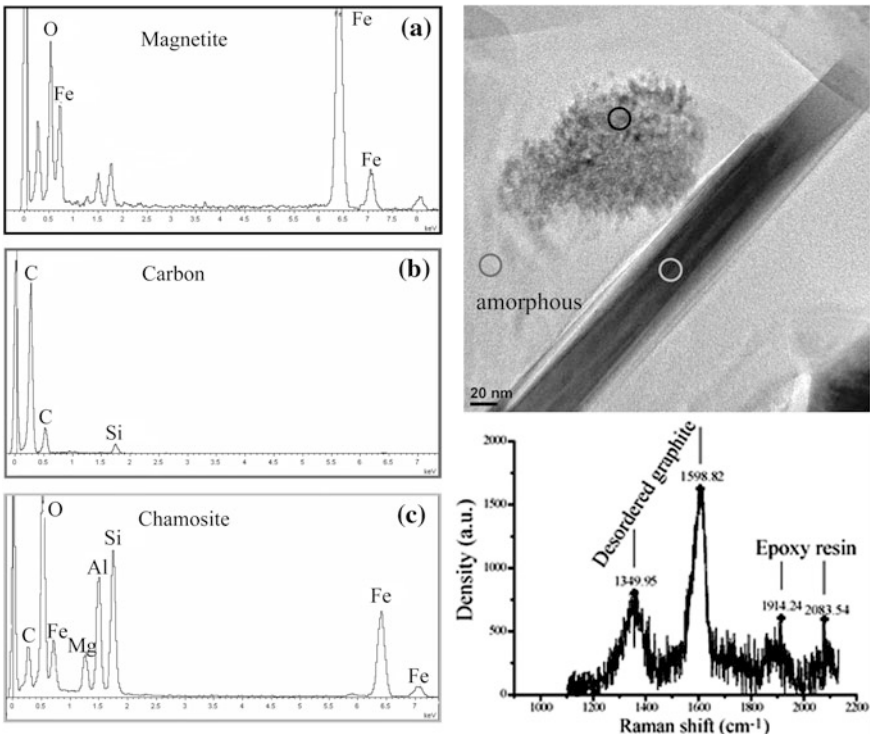

Fig. 6.18 TEM image of the chlorite fibers and precipitated magnesite surrounded by amorphous and poorly crystallized carbon. *On the left* Chemical analysis associated with the TEM image, **a** magnetite chemical analysis, **b** carbon chemical analysis and **c** chamosite chemical analysis. Raman spectra of precipitated carbon near chlorite compared with epoxy-resin spectra and disordered carbon spectra (from Luquot et al. 2012)

observed that different reaction processes took place depending on the transport conditions. First, they concluded that dolomite and ankerite dissolution (the two main minerals displaying fast kinetics) was controlled the hydrodynamic transport of the reactants; second, they observed that dissolution processes were rather homogeneous at high flow rates whereas the dissolution pattern appears to be more localized (wormhole-like) for the lowest flow rate injection experiments; third, permeability increases during all experiments, regardless of flow rate and brine type, but at high flow rates, some particles were apparently dragged through the samples, causing sporadic decreases in permeability due to local pore clogging. Furthermore it was observed that the precipitation of the secondary minerals (kaolinite, muscovite and smectite) as well as the dissolution of K-feldspar was larger at low flow rate injection than at high flow rate. The authors attributed this behavior to dissolution/precipitation localization mechanisms in the immobile zones where local chemical micro-environments may subsist.

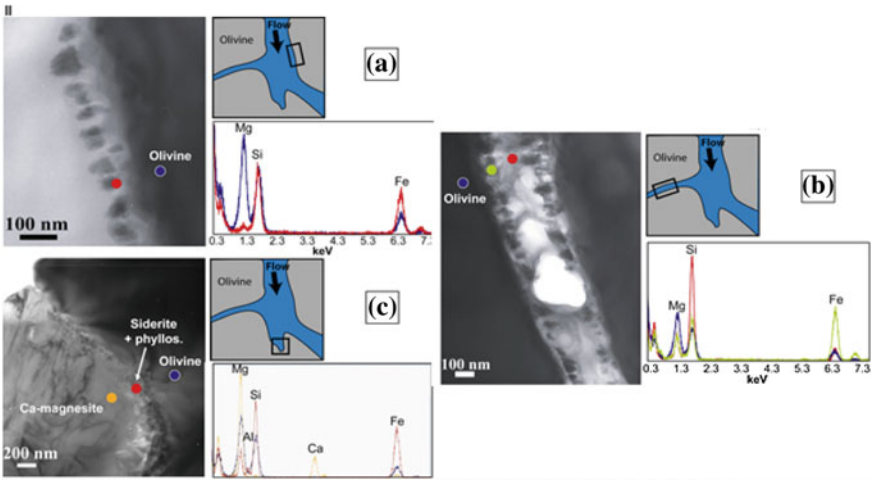

Fig. 6.19 TEM images of the main reaction textures (**a**–**c**) observed in the samples after the experiment end. For each reaction texture, a sketch diagram shows the main type of hydrodynamic zone in which the texture is observed and the corresponding reactants and products identified. This illustrates the variability of transport-reaction processes controlled by the structural heterogeneity of the sample (from Andreani et al. 2009)

The conclusions we can draw from this set of experimental results are:

- For the duration of the experiments, the changes in porosity, permeability and reactive surface area values caused by the dissolution reactions are controlled by the composition of the injected fluid but also by the initial properties of the rock; a memory effect of the initial heterogeneity of the samples has been observed in the variation of all these parameters with time.
- These experiments are quite unique for evaluating the permeability-porosity relationship associated with the dissolution process, while permeability-porosity relationships are generally obtained from cross-plotting permeability and porosity values measured on sets of sampled rock, i.e. not considering the dynamic of the process.
- One can speculate that the porosity–permeability relationship can be parametrized at first order by the effective hydraulic diameter and tortuosity changes triggered by the rock-forming mineral dissolution. Porosity–permeability relationship associated with precipitation mechanisms is presently not settled.
- The type of reactions experimented here cannot be modeled easily by a continuum approach. Local chemical environments triggering strong local concentration gradients at pore scale triggered by the heterogeneity of the velocity field and consequently the spatial variability of the local values of the *Pe* and *Da* numbers.

References

Akin S, Kovscek AR (1999) Imbibition studies of low-permeability porous media. Society of Petroleum Engineers

Al-Bulushi IR, Al-Maamari RS, Wilson OB (2012) Brine versus Klinkenberg corrected gas permeability correlation for Shuaiba carbonate formation. J Pet Sci Eng 92–93:24–29

Andreani M, Luquot L, Gouze P, Godard M, Hoisé E, Gibert B (2009) Experimental alteration of peridotite during injection of CO_2-rich fluids. Environ Sci Technol 43:1226–1231

Andrew M, Bijeljic B, Blunt MJ (2014) Pore-scale imaging of trapped supercritical carbon dioxide in sandstones and carbonates. Int J Greenh Gas Control 22:1–14

Bear J (1972) Dynamics of fluids in porous media. American Elsevier, New York, NY

Berg S, Oedai S, Ott H (2013) Displacement and mass transfer between saturated and unsaturated CO_2–brine systems in sandstone. Int J Greenh Gas Control 12:478–492

Berkowitz B, Scher H, Silliman SE (2000) Anomalous transport in laboratory-scale, heterogeneous porous media. Water Resour Res 36:149–158

Birkholzer JT, Cihan A, Zhou Q (2012) Impact-driven pressure management via targeted brine extraction—conceptual studies of CO_2 storage in saline formations. Int J Greenh Gas Control 7:168–180

Bloomfield JP, Williams AT (1995) An empirical liquid permeability–gas permeability correlation for use in aquifer properties studies. Q J Eng Geol Hydrogeol 28:S143–S150

Brooks RH, Corey AT (1966) Properties of porous media affecting fluid flow. J Irrig Drain Div 92:61–88

Brooks RH, Corey AT (1964) Hydraulic properties of porous media. Colorado State University, Colorado

Brunauer S, Emmett PH, Teller E (1938) Adsorption of gases in multimolecular layers. J Am Chem Soc 60:309–319

Burnside NM, Naylor M (2014) Review and implications of relative permeability of CO_2/brine systems and residual trapping of CO_2. Int J Greenh Gas Control 23:1–11

Carroll S, Hao Y, Smith M, Sholokhova Y, (2013) Development of scaling parameters to describe CO_2–rock interactions within Weyburn–Midale carbonate flow units. Int J Greenh Gas Control, The IEAGHG Weyburn-Midale CO_2 Monitoring and Storage Project 16, suppl. 1, S185–S193

Chang YC, Mohanty KK, Huang DD, Honarpour MM (1997) The impact of wettability and core-scale heterogeneities on relative permeability. J Pet Sci Eng 18:1–19

Chierici GL (1984) Novel relations for drainage and imbibition relative permeabilities. Soc Pet Eng J 24:275–276

Chiquet P, Broseta D, Thibeau S (2007) Wettability alteration of caprock minerals by carbon dioxide. Geofluids 7:112–122

Clennell MB (1997) Tortuosity: a guide through the maze. Geol Soc Lond Spec Publ 122:299–344

Coates GR, Denoo SA (1980) Log derived mechanical properties and rock stress. Presented at the SPWLA 21st annual logging symposium, Society of Petrophysicists and Well-Log Analysts

Corey AT (1954) The interrelation between gas and oil relative permeabilities. Producers Monthly 19:38–41

Cortis A, Berkowitz B (2004) Anomalous transport in "classical" soil and sand columns. Soil Sci Soc Am J 68:1539–1548

Crank J (1975) The mathematics of diffusion. Clarendon Press, Oxford

Cueto-Felgueroso L, Juanes R (2016) A discrete-domain description of multiphase flow in porous media: Rugged energy landscapes and the origin of hysteresis. Geophys Res Lett 43

Cui X, Bustin AMM, Bustin RM (2009) Measurements of gas permeability and diffusivity of tight reservoir rocks: different approaches and their applications. Geofluids 9:208–223

Daccord G, Lenormand R, Liétard O (1993) Chemical dissolution of a porous medium by a reactive fluid—I. Model for the "wormholing" phenomenon. Chem Eng Sci 48:169–178

Dake L (1978) Fundamentals of reservoir engineering. Elsevier, Amsterdam

Dandekar AY (2013) Petroleum reservoir rock and fluid properties, 2nd edn. CRC Press, Taylor & Francis Group, New York

Dentz M, Gouze P, Russian A, Dweik J, Delay F (2012) Diffusion and trapping in heterogeneous media: an inhomogeneous continuous time random walk approach. Adv Water Resour 49:13–22

Duan Z, Sun R, Zhu C, Chou I-M (2006) An improved model for the calculation of CO_2 solubility in aqueous solutions containing Na^+, K^+, Ca^{2+}, Mg^{2+}, Cl^-, and SO_4^{2-}. Mar Chem 98:131–139

Durner W (1994) Hydraulic conductivity estimation for soils with heterogeneous pore structure. Water Resour Res 30:211–223

Ebeltoft E, Lomeland F, Brautaset A, Haugen Å (2014). Parameter based scal-analysing relative permeability for full field application. In: International Symposium of the Society of Core Analysis, Avignon, France, 8–11 Sep 2014

Edlmann K, Somerville JM, Smart BGD, Hamilton SA, Crawford BR (1998) Predicting rock mechanical properties from wireline porosities. Society of Petroleum Engineers, Norway

Edlmann K, Haszeldine S, McDermott C (2013) Experimental investigation into the sealing capability of naturally fractured shale caprocks to supercritical carbon dioxide flow. Environ Earth Sci 70(7): 3393-3409.-17

Fischer G (1992) The determination of permeability and storage capacity: pore pressure oscillation method. In: Wong T, Evans B (eds) Fault mechanics and transport properties of rocks. Academic Press, New York, pp 187–211

Fjar E, Holt RM, Raaen AM, Risnes R, Horsrud P (1992) Petroleum related rock mechanics. Elsevier Science, London

Garrouch AA, Ali L, Qasem F (2001) Using diffusion and electrical measurements to assess tortuosity of porous media. Ind Eng Chem Res 40:4363–4369

Gassman F (1951) Uber die elastizitat poroser mediem. Vier der Natur, Gresellschaft in Zurich 1–23

Georgiadis A, Maitland G, Trusler JPM, Bismarck A (2010) Interfacial tension measurements of the (H_2O + CO_2) system at elevated pressures and temperatures. J Chem Eng Data 55:4168–4175

Gharbi O (2014) Fluid–rock interactions in carbonates; applications to CO_2 storage. Imperial College

Giesche H (2006) Mercury porosimetry: a general (practical) overview. Part Part Syst Charact 23:9–19

Gjetvaj F, Russian A, Gouze P, Dentz M (2015) Dual control of flow field heterogeneity and immobile porosity on non-Fickian transport in Berea sandstone. Water Resour Res 51:8273–8293

Glover P (2009) What is the cementation exponent? A new interpretation. Lead Edge 28:82–85

Golfier F, Zarcone C, Bazin B, Lenormand R, Lasseux D, Quintard M (2002) On the ability of a Darcy-scale model to capture wormhole formation during the dissolution of a porous medium. J Fluid Mech 457:213–254

Gouze P, Le Borgne T, Leprovost R, Lods G, Poidras T, Pezard P (2008) Non-Fickian dispersion in porous media: 1. Multiscale measurements using single-well injection withdrawal tracer tests. Water Resour Res 44:W06426

Gouze P, Leprovost R, Poidras T, Le Borgne T, Lods G, Pezard PA (2009) CoFIS and TELog: new downhole tools for characterizing dispersion processes in aquifers by single-well injection-withdrawal tracer tests. Comptes Rendus Geosci Hydrogeophys 341, 965–975

Gouze P, Luquot L (2011) X-ray microtomography characterization of porosity, permeability and reactive surface changes during dissolution. J Contam Hydrol. Reactive Transport in the Subsurface: Mixing, Spreading and Reaction in Heterogeneous Media 120–121, 45–55

Guarracino L, Rötting T, Carrera J (2014) A fractal model to describe the evolution of multiphase flow properties during mineral dissolution. Adv Water Resour 67:78–86

Haines WB (1930) Studies in the physical properties of soil. V. The hysteresis effect in capillary properties, and the modes of moisture distribution associated therewith. J Agric Sci 20:97–116

Halvorsen C, Hurst A (1990) Principles, practice and applications of laboratory minipermeametry. In: Worthington P (ed) Advances in core evaluation: accuracy and precision in reserves estimation, pp 521–549

Hamouda AA, Karoussi O, Chukwudeme EA (2008) Relative permeability as a function of temperature, initial water saturation and flooding fluid compositions for modified oil-wet chalk. J Pet Sci Eng 63:61–72

Hassanizadeh SM, Gray WG (1993) Thermodynamic basis of capillary pressure in porous media. Water Resour Res 29:3389–3405

Hidalgo JJ, Carrera J (2009) Effect of dispersion on the onset of convection during CO_2 sequestration. J Fluid Mech 640:441

Hilfer R, Øren PE (1996) Dimensional analysis of pore scale and field scale immiscible displacement. Transp Porous Media 22:53–72

Hingerl FF, Yang F, Pini R, Xiao X, Toney MF, Liu Y, Benson SM (2016) Characterization of heterogeneity in the Heletz sandstone from core to pore scale and quantification of its impact on multi-phase flow. Int J Greenh Gas Control

Hoefner ML, Fogler HS (1988) Pore evolution and channel formation during flow and reaction in porous media. AIChE J 34:45–54

Hoek E, Franklin JA (1968) Simple triaxial cell for field or laboratory testing of rock. Trans Inst Min Met 77:A22–A26

Honarpour M, Koederitz L, Harvey AH (1986) Relative permeability of petroleum reservoirs. CRC Press, Boca Raton

Hossain Z (2012) Rock physics modeling of CO_2 bearing reservoir rocks. Society of Petroleum Engineers, Denmark

Huang DD, Honarpour MM (1998) Capillary end effects in coreflood calculations. J Pet Sci Eng 19:103–117

Iglauer S, Paluszny A, Pentland CH, Blunt MJ (2011) Residual CO_2 imaged with X-ray micro-tomography. Geophys Res Lett 38:L21403

Iglauer S, Pentland CH, Busch A (2015) CO_2 wettability of seal and reservoir rocks and the implications for carbon geo-sequestration. Water Resour Res 51:729–774

Jaeger J, Cook NG, Zimmerman R (2007) Fundamentals of rock mechanics, 4th edn. Wiley-Blackwell, Malden, MA

Johnson EF, Bossler DP, Naumann VO (1959) Calculation of relative permeability from displacement experiments 216:370–372

Jones SC, Roszelle WO (1978) Graphical techniques for determining relative permeability from displacement experiments. J Pet Technol 30:807–817

Juanes R, Spiteri EJ, Orr FM, Blunt MJ (2006) Impact of relative permeability hysteresis on geological CO_2 storage. Water Resour Res 42:W12418

Kamath J, de Zabala EF, Boyer RE (1995) Water/Oil Relative permeability endpoints of intermediate-wet, low-permeability rocks. SPE Form Eval 10:4–10

Klinkenberg LJ (1941) The permeability of porous media to liquids and gases. Presented at the Drilling and Production Practice, American Petroleum Institute, pp 200–213

Kosugi K 'ichirou (1996) Lognormal distribution model for unsaturated soil hydraulic properties. Water Resour Res 32:2697–2703

Krevor SCM, Pini R, Zuo L, Benson SM (2012) Relative permeability and trapping of CO_2 and water in sandstone rocks at reservoir conditions. Water Resour Res 48:W02532

Lasaga AC (1998) Kinetic theory in the earth sciences. Princeton University Press, New Jersey, 811p

Lee TC, Kashyap RL, Chu CN (1994) Building skeleton models via 3-D medial surface axis thinning algorithms CVGIP Graph. Models Image Process 56:462–478

Leverett MC (1941) Capillary behavior in porous solids. Trans AIME 142:152–169

Levine JS, Goldberg DS, Lackner KS, Matter JM, Supp MG, Ramakrishnan TS (2014) Relative permeability experiments of carbon dioxide displacing brine and their implications for carbon sequestration. Environ Sci Technol 48:811–818

Levy M, Berkowitz B (2003) Measurement and analysis of non-Fickian dispersion in heterogeneous porous media. J Contam Hydrol 64:203–226

Li K, Horne RN (2006) Comparison of methods to calculate relative permeability from capillary pressure in consolidated water-wet porous media. Water Resour Res 42:W06405

Li K, Horne RN (2002) Experimental verification of methods to calculate relative permeability using capillary pressure data. Society of Petroleum Engineers

Lindquist WB, Venkatarangan A (1999) Investigating 3D geometry of porous media from high resolution images. Phys Chem Earth Part Solid Earth Geod 24:593–599

Lomeland F, Ebeltoft E, Thomas WH (2005) A new versatile relative permeability correlation. In: International Symposium of the Society of Core Analysts, Toronto, Canada, pp 21–25

Lu B, Torquato S (1993) Chord-length and free-path distribution functions for many-body systems. J Chem Phys 98:6472–6482

Luquot L, Andreani M, Gouze P, Camps P (2012) CO_2 percolation experiment through chlorite/zeolite-rich sandstone (Pretty Hill Formation—Otway Basin–Australia). Chem Geol 294–295:75–88

Luquot L, Gouze P (2009) Experimental determination of porosity and permeability changes induced by injection of CO_2 into carbonate rocks. Chem Geol. CO_2 geological storage: Integrating geochemical, hydrodynamical, mechanical and biological processes from the pore to the reservoir scale 265, 148–159

Luquot L, Gouze P, Niemi A, Bensabat J, Carrera J (2016) CO_2-rich brine percolation experiments through Heletz reservoir rock samples (Israel): role of the flow rate and brine composition. Int J Greenh Gas Control

Luquot L, Rodriguez O, Gouze P (2014) Experimental characterization of porosity structure and transport property changes in limestone undergoing different dissolution regimes. Transp Porous Media 101:507–532

Mathias SA, Gluyas JG, de Miguel GJGM, Bryant SL, Wilson D (2013) On relative permeability data uncertainty and CO_2 injectivity estimation for brine aquifers. Int J Greenh Gas Control 12:200–212

McCraw C, Edlmann K, Miocic J, Gilfillan S, Haszeldine RS, McDermott CI (2016) Experimental investigation and hybrid numerical analytical hydraulic mechanical simulation of supercritical CO_2 flowing through a natural fracture in caprock. Int J Greenh Gas Control 48:120–133. http://www.sciencedirect.com/science/article/pii/S1750583616300020

Meijster A, Roerdink JBTM, Hesselink WH (2002) A general algorithm for computing distance transforms in linear time. In: Goutsias J, Vincent L, Bloomberg DS (eds) Mathematical morphology and its applications to image and signal processing, computational imaging and vision. Springer, Berlin, pp 331–340

Metwally YM, Sondergeld CH (2011) Measuring low permeabilities of gas-sands and shales using a pressure transmission technique. Int J Rock Mech Min Sci 48:1135–1144

Moebius F, Or D (2012) Interfacial jumps and pressure bursts during fluid displacement in interacting irregular capillaries. J Colloid Interface Sci 377:406–415

Moghadasi L, Guadagnini A, Inzoli F, Bartosek M (2015) Interpretation of two-phase relative permeability curves through multiple formulations and Model Quality criteria. J Pet Sci Eng 135:738–749

Morita N, Whitfill DL, Massie I, Knudsen TW (1987) Realistic sand production prediction. In: SPE 16989 62nd Annual Technical Conference and Exhibition. Presented at the The SPE Dallas 1987

Morrow NR (1970) Physics and thermodynamics of capillary action in porous media. Ind Eng Chem 62:32–56

Navarre-Sitchler A, Steefel CI, Yang L, Tomutsa L, Brantley SL (2009) Evolution of porosity and diffusivity associated with chemical weathering of a basalt clast. J Geophys Res Earth Surf 114

Nikolaidis N, Pitas I (2001) 3-D image processing algorithms. Wiley-Interscience, New York

Noiriel C, Gouze P, Bernard D (2004) Investigation of porosity and permeability effects from microstructure changes during limestone dissolution. Geophys Res Lett 31:1–4

Noiriel C, Luquot L, Madé B, Raimbault L, Gouze P, van der Lee J (2009) Changes in reactive surface area during limestone dissolution: an experimental and modelling study. Chem Geol 265:160–170

Oikawa Y, Takehara T, Tosha T (2008) Effect of CO_2 injection on mechanical properties of berea sandstone. In: Presented at the The 42nd U.S. Rock Mechanics Symposium (USRMS), American Rock Mechanics Association

Pan C, Hilpert M, Miller CT (2001) Pore-scale modeling of saturated permeabilities in random sphere packings. Phys Rev E 64:66702

Pentland CH, El-Maghraby R, Iglauer S, Blunt MJ (2011) Measurements of the capillary trapping of super-critical carbon dioxide in Berea sandstone. Geophys Res Lett 38:L06401

Perrin J-C, Benson S (2010) An experimental study on the influence of sub-core scale heterogeneities on CO_2 distribution in reservoir rocks. Transp Porous Media 82:93–109

Pinder GF, Gray WG (2008) Essentials of multiphase flow in porous media, 1st edn. Wiley-Interscience, Hoboken, NJ

Pini R, Benson SM (2013) Simultaneous determination of capillary pressure and relative permeability curves from core-flooding experiments with various fluid pairs. Water Resour Res 49:3516–3530

Pinter A, Bodi T (2012) Determination of capillary pressure and relative permeability curves with a novel ultra rock centrifuge. Geosci Eng 1:75–86

Pokrovsky OS, Golubev SV, Schott J, Castillo A (2009) Calcite, dolomite and magnesite dissolution kinetics in aqueous solutions at acid to circumneutral pH, 25 to 150 °C and 1 to 55 atm P_{CO_2}: new constraints on CO_2 sequestration in sedimentary basins. Chem. Geol., CO_2 geological storage: Integrating geochemical, hydrodynamical, mechanical and biological processes from the pore to the reservoir scale 265, 20–32

Purcell WR (1949) Capillary pressures—their measurement using mercury and the calculation of permeability therefrom. J Pet Technol 1:39–48

Rahman T, Lebedev M, Barifcani A, Iglauer S (2016) Residual trapping of supercritical CO_2 in oil-wet sandstone. J Colloid Interface Sci 469:63–68

Ramakrishnan TS, Cappiello A (1991) A new technique to measure static and dynamic properties of a partially saturated porous medium. Chem Eng Sci 46:1157–1163

Rashid F, Glover PWJ, Lorinczi P, Collier R, Lawrence J (2015) Porosity and permeability of tight carbonate reservoir rocks in the north of Iraq. J Pet Sci Eng 133:147–161

Rege SD, Fogler HS (1987) Network model for straining dominated particle entrapment in porous media. Chem Eng Sci 42:1553–1564

Renard F, Gratier J-P, Ortoleva P, Brosse E, Bazin B (1998) Self-organization during reactive fluid flow in a porous medium. Geophys Res Lett 25:385–388

Riaz A, Hesse M, Tchelepi HA, Orr FM (2006) Onset of convection in a gravitationally unstable diffusive boundary layer in porous media. J Fluid Mech 548:87–111

Risnes R, Bratli RK, Horsrud P (1982) Sand stresses around a wellbore. Soc Pet Eng J 22:883–898

Russian A, Dentz M, Gouze P (2016) Time domain random walks for hydrodynamic transport in heterogeneous media. Water Resour Res

Sahimi M (2011) Flow and transport in porous media and fractured rock: from classical methods to modern approaches, 2nd edn. New York, Wiley

Sarda J-P, Kessler N, Wicquart E, Hannaford K, Deflandre J-P (1993) Use of porosity as a strength indicator for sand production evaluation. Society of Petroleum Engineers

Schechter RS, Gidley JL (1969) The change in pore size distribution from surface reactions in porous media. AIChE J 15:339–350

Scheidegger AE (1974) The physics of flow through porous media, 3rd edn. University of Toronto Press, Toronto, Buffalo NY

Schlüter S, Sheppard A, Brown K, Wildenschild D (2014) Image processing of multiphase images obtained via X-ray microtomography: a review. Water Resour Res 50:3615–3639

Seki K (2007) SWRC fit a nonlinear fitting program with a water retention curve for soils having unimodal and bimodal pore structure. Hydrol Earth Syst Sci Discuss 4:407–437

Sen PN (2004) Time-dependent diffusion coefficient as a probe of geometry. Wiley Subscr Serv Inc Wiley Co 23A:1–21

Siddiqi K, Pizer SM (eds) (2008) Medial representations, computational imaging and vision. Springer, Dordrecht

Silin D, Tomutsa L, Benson SM, Patzek TW (2011) Microtomography and pore-scale modeling of two-phase fluid distribution. Transp Porous Media 86:495–515
Smart BDG, Somerville JM, Crawford BR (1999) A rock test cell with true triaxial capability. Geotech Geol Eng 17:157–176
Stein N, Hilchie DW (1972) Estimating the maximum sand free production rates from friable sandstones without using sand control. J Pet Technol
Stein N, Odeh AS, Jones LG (1974) Estimating maximum sand free production rates from friable sandstones for different well completion geometries. J Pet Technol
Succi S (2001) The Lattice Boltzmann equation for fluid dynamics and beyond, numerical mathematics and scientific computation. Oxford University Press, Oxford
Sun R, Dubessy J (2010) Prediction of vapor–liquid equilibrium and PVTx properties of geological fluid system with SAFT-LJ EOS including multi-polar contribution. Part I: Application to H_2O–CO_2 system. Geochim Cosmochim Acta 74:1982–1998
Tenchine S, Gouze P (2005) Density contrast effects on tracer dispersion in variable aperture fractures. Adv Water Resour 28:273–289
Tinker PB (1969) A steady-state method for determining diffusion coefficients in soil. J Soil Sci 20:336–345
Tixier MP, Loveless GW, Anderson RA (1975) Estimation of formation strength from the mechanical-properties log. J Pet Technol 27:283–293
Torquato S (2002) Random heterogeneous materials. Interdisciplinary applied mathematics. Springer, New York
van Brakel J, Heertjes PM (1974) Analysis of diffusion in macroporous media in terms of a porosity, a tortuosity and a constrictivity factor. Int J Heat Mass Transf 17:1093–1103
van Genuchten M (1980) A closed-form equation for predicting the hydraulic conductivity of unsaturated soils. Soil Sci Soc Am J 44:892–898
Van Loon LR, Soler JM, Jakob A, Bradbury MH (2003) Effect of confining pressure on the diffusion of HTO, $36Cl^-$ and $125I^-$ in a layered argillaceous rock (Opalinus Clay): diffusion perpendicular to the fabric. Appl Geochem 18:1653–1662
Virnovsky GA, Skjaeveland SM, Surdal J, Ingsoy P (1995) Steady-state relative permeability measurements corrected for capillary effects. Society of Petroleum Engineers
Wang S, Edwards IM, Clarens AF (2012) Wettability phenomena at the CO_2–brine–mineral interface: implications for geologic carbon sequestration. Environ Sci Technol 47:234–241
Washburn EW (1921) The dynamics of capillary flow. Phys Rev 17:273–283
Weingarten JS, Perkins TK (1992) Prediction of sand production in gas wells: methods and gulf of mexico case studies. Presented at the SPE Annual Technical Conference and Exhibition, Washington
Welge HJ (1952) A simplified method for computing oil recovery by gas or water drive. J Pet Technol 4:91–98
Wojtacki K, Lewandowska J, Gouze P, Lipkowski A (2015) Numerical computations of rock dissolution and geomechanical effects for CO_2 geological storage. Int J Numer Anal Methods Geomech 39:482–506
Wu Y-S, Pruess K, Persoff P (1998) Gas flow in porous media with Klinkenberg effects. Transp Porous Media 32:117–137
Zhang H, He S, Jiao C, Luan G, Mo S, Guo X (2014) Determination of dynamic relative permeability in ultra-low permeability sandstones via X-ray CT technique. J Pet Explor Prod Technol 4:443–455
Zhang Y, Li H, Yang D (2012) Simultaneous estimation of relative permeability and capillary pressure using ensemble-based history matching techniques. Transp Porous Media 94:259–276
Zhu Z, Li M, Lin M, Peng B, Sun L, Chen L (2011) Investigation on variations in wettability of reservoir rock induced by CO_2-brine-rock interactions. Society of Petroleum Engineers, SPE-142979-MS